Influence of Clay-Containing Sediments on Methane Hydrate Formation: Impacts on Kinetic Behavior and Gas Storage Capacity

Constant Art-Clarie Agnissan, Charlène Guimpier, Marco Terzariol, Olivia Fandino, Sandrine Chéron, Vincent Riboulot, Arnaud Desmedt, Livio Ruffine

To cite this version:

Constant Art-Clarie Agnissan, Charlène Guimpier, Marco Terzariol, Olivia Fandino, Sandrine Chéron, et al.. Influence of Clay-Containing Sediments on Methane Hydrate Formation: Impacts on Kinetic Behavior and Gas Storage Capacity. Journal of Geophysical Research : Solid Earth, 2023, 128 (9), e2023JB027333 (22p.). 10.1029/2023JB027333 . hal-04204149

HAL Id: hal-04204149
https://hal.science/hal-04204149v1

Submitted on 21 Oct 2024

JGR Solid Earth

RESEARCH ARTICLE
10.1029/2023JB027333

Key Points:

- Clay content and clay mineralogy significantly affect the induction time of methane hydrate formation as well as the hydrate morphology
- Illite-rich clays reduce the cage occupancy of hydrates and thus the resulting gas storage capacity (GSC)
- Microscale analyses underpins the need to characterize microscopic properties of hydrates to estimate GSC

Supporting Information:

Supporting Information may be found in the online version of this article.

Correspondence to:

L. Ruffine and A. Desmedt,
livio.ruffine@ifremer.fr;
arnaud.desmedt@u-bordeaux.fr

Citation:

Constant Agnissan, A.-C., Guimpier, C., Terzariol, M., Fandino, O., Chéron, S., Riboulot, V., et al. (2023). Influence of clay-containing sediments on methane hydrate formation: Impacts on kinetic behavior and gas storage capacity. *Journal of Geophysical Research: Solid Earth*, *128*, e2023JB027333. https://doi.org/10.1029/2023JB027333

Received 29 JUN 2023
Accepted 15 AUG 2023

Author Contributions:

Conceptualization: Art-Clarie Constant Agnissan, Olivia Fandino, Livio Ruffine
Data curation: Art-Clarie Constant Agnissan, Charlène Guimpier, Arnaud Desmedt
Formal analysis: Art-Clarie Constant Agnissan, Charlène Guimpier, Olivia Fandino, Sandrine Chéron
Funding acquisition: Vincent Riboulot, Arnaud Desmedt, Livio Ruffine
Investigation: Art-Clarie Constant Agnissan, Marco Terzariol, Olivia Fandino, Vincent Riboulot, Arnaud Desmedt, Livio Ruffine
Methodology: Art-Clarie Constant Agnissan, Charlène Guimpier, Olivia Fandino, Arnaud Desmedt, Livio Ruffine
Project Administration: Vincent Riboulot

Influence of Clay-Containing Sediments on Methane Hydrate Formation: Impacts on Kinetic Behavior and Gas Storage Capacity

Art-Clarie Constant Agnissan[1,2], Charlène Guimpier[1,2,3], Marco Terzariol[1], Olivia Fandino[1], Sandrine Chéron[1], Vincent Riboulot[1], Arnaud Desmedt[2], and Livio Ruffine[1,4]

[1]Ifremer, University Brest, CNRS, UMR Geo-Ocean, Plouzané, France, [2]Groupe Spectroscopie Moléculaire, ISM, UMR 5255, CNRS, University de Bordeaux, Talence, France, [3]SLAC - SLAC National Accelerator Laboratory, Stanford University, Menlo Park, CA, USA, [4]Now at IFPEN, Rueil-Malmaison, France

Abstract On Earth, natural hydrates are mostly encountered in clay-rich sediments. Yet their formation processes in such matrices remain poorly understood. Achieving an in-depth understanding of how methane hydrates accumulate on continental margins is key to accurately assess (a) their role in sustaining the development of some chemosynthetic communities at cold seeps, (b) their potential in terms of energy resources and geohazards, and (c) the fate of the methane releases, a powerful greenhouse gas, in this changing climate. This study investigated the formation of methane hydrates and their gas storage capacity (GSC) in clay-rich sediments. A set of hydrate experiments were performed in matrices composed of sand, illite-rich clay, and montmorillonite-rich clay at different proportions aiming to determine the role of mineralogy on hydrate formation processes. The experiments demonstrate that a clay content of 10% in a partially water saturated sand/clay mixture increases the induction time by ∼60%, irrespective of the nature of the clay used. The increase in water saturation in the two matrices promotes hydrate formation. Micro-Raman spectroscopic analyses reveal that increasing the clay content leads to a decrease in the hydrate small-cage occupancy, with an impact on the storage capacity. Finally, the analyses of collected natural samples from the Black Sea (off Romania) enable us to estimate the GSC of the deposit. Our estimates is different from previous ones, and supports the importance of coupling multiscale properties, from the microscale to the geological scale, to accurately assess the total amount of methane hosts in hydrate deposits worldwide.

Plain Language Summary Natural gas hydrates are amongst the largest methane reservoirs on Earth. They are sensitive to temperature increase. Societal and environmental concerns surrounding natural gas hydrates pertain to their decomposition, and in particular to the amount of gas they may release and its fate: can it trigger geohazards, or jeopardize the development of unique chemosynthetic communities encountered on continental margins? In-depth knowledge of hydrate formation processes and properties are essential to provide reliable answers to these questions. The majority of hydrate deposits are characterized by clay-rich sediments. We led a comprehensive study coupling fine microstructural analyses of both natural and synthetic hydrate samples with macroscale laboratory experiments within different matrices to show how clays can affect their formation kinetics and storage capacity. We found that even a small amount of clay can significantly change the formation kinetics of hydrates, and the matrix mineralogy affects their storage capacity. This study is crucial with a view to accurately assessing the amount of methane trapped in hydrate deposits, and for improved prediction of the consequences of their decomposition on the environment in a changing climate.

1. Introduction

Gas hydrates are crystalline compounds in which gas molecules are trapped in cavities called cages formed by water molecules (Desmedt et al., 2012; Ruffine et al., 2018; Sloan & Koh, 2007). The most naturally occurring form of hydrates corresponds to deposits where methane (CH_4) is overwhelmingly present (more that 99%-mol) (Kvenvolden, 1998). On Earth, they are widely distributed in both the permafrost regions and marine sediments along the continental margins as their formation is governed by low-temperature and high-pressure conditions (Koh et al., 2012; You et al., 2019). Accordingly, they are very sensitive to climate change. Their decomposition on continental margins may affect both seabed stability (Sultan et al., 2004) and the development of autochthonous chemosynthetic communities (Levin, 2005; MacDonald et al., 2003), whereas in permafrost, part of the

Supervision: Arnaud Desmedt, Livio Ruffine
Validation: Art-Clarie Constant Agnissan, Olivia Fandino, Arnaud Desmedt, Livio Ruffine
Writing – original draft: Art-Clarie Constant Agnissan
Writing – review & editing: Art-Clarie Constant Agnissan, Marco Terzariol, Olivia Fandino, Livio Ruffine

methane released is transferred to the atmosphere and making these deposits a potential contributor to global warming (Dickens et al., 1997; Kennett et al., 2003; Ruppel & Kessler, 2017).

Natural gas hydrates are well known for their high gas-storage capacity, making them the most important methane reservoir on earth, with estimates ranging from 3–5 × 10^{15} (Boswell & Collett, 2011; Milkov, 2004; Wallmann et al., 2012) to 3 × 10^{18} m^3 (Trofimuk et al., 1975). This huge amount of methane is regarded as an opportunity for countries with limited energy resources to meet their internal and external energy demands (Hancock et al., 2005; Yamamoto et al., 2019). Furthermore, the high gas-storage capacity of hydrates opens a route to innovative development of (coupled)-processes related to seawater desalinization and/or gas storage, with potential applications in carbon capture, utilization and storage (CCUS) (Linga et al., 2007) and hydrogen storage (Nakayama et al., 2010).

Although natural gas hydrates have been investigated for decades, their formation and decomposition processes are still poorly understood, limiting our knowledge on their growth and distribution mechanisms in porous matrices in the natural environment. It is still unclear how sediment mineralogy quantitatively affects the growth kinetics and final distribution of gas hydrates. Yet, such properties are key to a quantitative insight into how fluid flows within a hydrate deposit; which is relevant in understanding community distribution over a hydrate deposit, assessing slope and seafloor stability, and developing reliable technologies for methane production. Besides, the kinetic behavior of hydrate formation is influenced by a variety of parameters associated with sediments such as particle and pore sizes, mineralogy, water saturation, and pore water chemistry (Malagar et al., 2019). These parameters affect the induction time (Benmesbah et al., 2020; S. Wang et al., 2016), the rate of hydrate growth and the water-hydrate conversion rate (Babu et al., 2013; Linga et al., 2009; Loh et al., 2012; Mekala et al., 2014). Therefore, to obtain in-depth knowledge on formation kinetics and the distribution of hydrates in porous matrices, it is important to investigate the influence of each of the aforementioned parameters separately. However, such an endeavor will lead to a huge amount of experiments to carry out. Therefore, the selection of key parameters to investigate is crucial. Moreover, most of natural gas hydrate deposits are hosted by silty and clayey sediments (Boswell & Collett, 2011; Boswell et al., 2020) and the mechanisms of hydrate formation in such fine-grained sediments are still poorly investigated at the lab scale. This is partly due to the difficulty in forming hydrate in poorly permeable clays (Chuvilin et al., 2002; Lei & Santamarina, 2018). From a mineralogy point of view, clays are hydrated aluminosilicates with a complex chemical and crystalline structure characterized by a stack of layers forming thin plate-like particles (Grim, 1962), whereas from a geotechnical ones, they represent sediment particles with sizes smaller than 2 or 4 μm (Das, 2008). These features result in a large specific surface area and small pores size (Das, 2008; Kumari & Mohan, 2021; Shmulovich et al., 1994), and gives rise to important physicochemical interactions in the presence of water such as adsorption, structural swelling and ionic exchanges, which can significantly affect the hydrate formation processes.

There are few studies what have focused on the influence of clay on the kinetics of hydrate formation in clay-rich matrices. Among them, Zeng et al. (2022), by studying methane hydrate formation in mixtures of silica sand and montmorillonite, found that at low montmorillonite content (10–25 wt %) the induction time is shortened, and it significantly increases when the montmorillonite content reaches 40 wt %. However, Zhang et al. (2017) showed that the addition of 10 wt % bentonite to a sand-clay matrix increases the induction time from 560 to 2,600 min and decreases the average hydrate growth rate by ∼50%. This inhibiting effect was attributed to restricted contact between gas and water resulting from the presence of fine clay particles between sandy grains. Likewise, Kumar et al. (2015) studied methane hydrate formation in different mixtures of sand and bentonite at various clay contents (25, 50, and 75 wt %) in a 500 cm^3 cylindrical reactor using the excess gas method. They found that even 25% of bentonite reduces the rate of hydrate formation by a factor of 4 compared to a matrix composed exclusively of sand. The lowest water to hydrate conversion rate was achieved for a sand/clay ratio of 25/75 wt %. They also investigated the influence of water saturation and noted that an increase in this parameter from 50% to 100% drastically reduced the rate of hydrate growth by a factor of 7 in a sand/clay mixture with a ratio 25/75 wt %. This has been related to better water-gas contact in a partially water-saturated sediment.

As mentioned above, there is a large discrepancy on the amount of methane trapped in these deposits, and very little attention has been paid to the potential influence of the nature of the host sediments on their structural characteristics, particularly on the occupancy of the large (θ_{LC}) and small (θ_{SC}) hydrate cages (Sloan & Koh, 2007). The cage occupancy is crucial in calculating the gas storage capacity (GSC), corresponding to the hydrate volumetric expansion factor (EF) at standard temperature and pressure (Boswell & Collett, 2011; Merey & Sinayuc, 2016). Accurate determination of this parameter will help in the reduction of uncertainties on the estimates of methane trapped within the hydrates. This is essential, not only in determining their potential as an energy resource or to assess seafloor/slope stability, but also to better constrain and predict their possible impact on climate change. Liu et al. (2008) carried out a study on hydrate structure by Raman spectroscopy, and they showed that the hydrate cage occupancy (θ_{LC} ~ 96.5% and θ_{LC} ~ 95%) is similar in bulk phase and in silica sands with particle sizes ranging from 53–75 to 150–180 μm. The physico-chemical interactions between water molecules and clays are directly related to their specific nature (surface area, interlayer cations, structural organization), and can in turn significantly affect host-guest interactions during hydrate formation (Davidson et al., 1987; Seol et al., 2010). For this reason, Yeon et al. (2011) investigated methane occupancy of natural hydrate in Na-montmorillonite using solid state ^{13}C MAS NMR and found that sodium (Na^+) cations were inserted into small cages (SC). This leads to values of relative cage occupancy ratios (θ_{LC}/θ_{SC}) as high as 2.4, thus far higher than the unity when small and large cages are completely filled. Such an occupancy of SC by Na^+ was observed in bulk propane hydrate by. Seol et al. (2012). Their results obtained in sand and clay illustrate the need for further experiments to better assess how and to what extent clayey sediments may affect cage occupancy.

The main goal of this work is to improve our understanding on the formation kinetics of methane hydrates in the presence of complex matrices containing sand, illite, and montmorillonite; and to assess how the sediment mineralogy affect hydrate storage capacity. The two aforementioned clays are characterized by very different chemical structures and swelling properties, and are commonly encountered in marine sediments (Fütterer, 2006), such as the hydrate-bearing sediments of the Western Black Sea (Chazallon et al., 2020; Ruffine et al., 2021). First, we investigated the effects of the nature and fraction of clays on the induction time and hydrate distribution. Different water saturations were applied in order to assess the importance of water content on hydrate formation. Second, Raman micro-spectroscopy has been performed on the synthesized hydrates to determine their cage occupancy and calculate their GSC. Finally, we compare the results with those obtained on the natural hydrate specimens collected on the Romanian margin of the Black Sea, and discuss the implications of the results regarding the estimation of the amount of CH_4 stored in the natural hydrate deposits of the Black Sea.

2. Materials and Methods

2.1. Materials

We selected Fontainebleau (FB) silica sand (Laboratoires Humeau, France), illite-rich clay (also called ILL in the following text) supplied by Argiletz Laboratoires (France) and Montmorillonite-rich clay K10 (called MMT hereafter) from Sigma Aldrich, as the porous media. Table 1 summarizes the semi-quantitative mineralogical analysis performed by X-ray diffraction (XRD). It shows that the matrix ILL contains ~60% clay, 24% quartz, while MMT is composed of 66% clay and 20% quartz.

Illite belongs to the 2:1 clay family in which the elementary aluminosilicate sheet is characterized by an octahedral (aluminum) layer sandwiched between two tetrahedral (silica) layers. The substitution of one Si^{4+} ion out of four by an Al^{3+} ion in the tetrahedral layers leads to a negative charge of the sheet which is compensated by the presence of K^+ cations in the interlayer space (Weil & Brady, 2017). The strong interactions between these anhydrous cations (K^+) confer a non-expansive behavior to illite in the presence of water. Montmorillonite belongs to the smectite group and it is also a 2:1 clay, like illite. They differ from each other mainly in the nature of interlayer counter-ions such as Na^+, Ca^{2+}, Mg^{2+} or Li^+ (Odom & Low, 1978; Weil & Brady, 2017), resulting in a larger internal specific surface area and a higher cation-exchange capacity relative to illite. The swelling capacity of the MMT K10 used in this study is reduced due to a chemical treatment applied by suppliers.

Fontainebleau Sand is 100% quartz, characterized by grain sizes between 80 and 450 μm (Figure 1). The clay matrices are composed of elongated platy grains (Figures 1a and 1b), with particle sizes ranging from 0.3 to 80 μm (mean size of 5 μm) and from 0.6 to 100 μm (mean diameter of 12.7 μm) for ILL and MMT, respectively (Figure 1c).

We used deionized water (18 MΩ cm at 25°C) degassed by ebullition prior to the experiment and methane with a purity of 99.995% supplied by Air Liquid.

2.2. Laboratory Methane Hydrate Formation in a High-Pressure Cell

2.2.1. Experimental Apparatus

The high-pressure apparatus used was designed to simulate upward gas transport as encountered at seeps in natural sedimentary environments. It allows the synthesis of small hydrate-bearing cores, while studying selected

Table 1
Main Properties of the Matrices Used in This Study

Property	Lllite-rich clay (ILL)	Montmorillonite-rich clay (MMT)	Sand FB	Characterization method
Particle size (D_{mean})	5.3 µm	12.7 µm	212 µm	Malvern Mastersizer 3,000 laser diffraction
Coefficient of uniformity (C_u)	4.53	5.93	1.55	$C_u = D_{60}/D_{10}$
Roundness (R)	–	–	0.4	
Specific surface (S_s)	66.4 m^2/g	240.8 m^2/g	0,01 m^2/g	ILL and MMT: N_2 BET adsorption measurements Sand: $S_s = 6/(G_s \times \rho_w \times D_{50})$ (Santamarina et al., 2001)
Global mineralogy				Sand: from supplier specifications
Quartz	29%	20%	100%	
Clays	56%	66%		
Calcite	13%	–		LL and MMT: X-ray diffraction using a D8 Advance BRÜKER-AXS
Gypsum	1%	–		
Plagioclase	–	14%		
Clay fraction mineralogy[a]				X-ray diffraction after separation of the clay fraction from the other components of the matrix
Smectite	<5%	82%		
Illite	77%	15%		
Kaolinite	17%	<5%		
Chlorite	<5%	<5%		

[a] Clay minerals have been separated from the rest of the matrix before XRD analyses, by a series of preparations and chemical treatments (Grim, 1962).

physicochemical parameters of the systems and/or key environmental factors that control their formation and decomposition processes.

Its detailed description is provided in Ruffine (2015) and its schematic diagram is shown in Figure 2. Briefly, it consists of a stainless steel high-pressure cylindrical cell (316-L) manufactured by TOP-Industrie (France). The cell measures 17 cm in height and 6 cm internal diameter with a volume of ~508 mL, and can be used at pressures up to 22 MPa and temperatures ranging from 253 to 373 K. Two flanges located at the top and the bottom hermetically seal the cell. Thermal regulation is ensured by fluid circulation using a thermostatic bath, Ministat 230 (Huber), through a jacket housing the cell. A 15-cm-long thermocouple type K with an uncertainty of ±0.2 K, inserted in the upper flange allows for temperature monitoring during experiments. Pressure is measured by a WIKA P-31 pressure transducer located at the bottom of the cell with an uncertainty of ±0.02 MPa. These two sensors are connected to a Eurotherm Chessel 6100E data logger that allows continuous data acquisition. Water and methane injection are controlled by a set of high-pressure mass flow and pressure regulators (Bronkhorst). The Bronkhorst Flow DDE, Flow View and Flow Plot softwares provide instrument control and data recording. Thus, the flow rate of water can be adjusted between 0.05 and 2.5 g min^{-1} with an accuracy of 1% of the full scale (FS), and gas-flow rate from 10 to 500 mLn min^{-1} with an accuracy of 0.1% of FS.

2.2.2. Experimental Procedure

We prepared matrices of pure sand, clay matrix/sand (ILL/sand/and MMT/sand) with clay content up to 60%, and ILL/MMT at ~60% clay. The mixtures were prepared by weighing, taking into account the fact that the ILL and MMT clay matrices are not entirely composed of clay minerals (Table 1). Thus, the proportions of each mixture component (ILL/sand, MMT/sand, and ILL/MMT) were determined according to the desired clay content. The mass ratios of clay matrix/sand and the corresponding clay contents are given in Table 2. It is therefore necessary to make the link between the clay content (fraction of clay minerals) in a mixture, and the proportion of the clay matrix (MMT or ILL) in that mixture.

The prepared matrix was either introduced by gravity directly into the high-pressure cell or into a cylindrical aluminum cell that is inserted afterward in the high-pressure cell (Figure S1 in Supporting Information S1). The

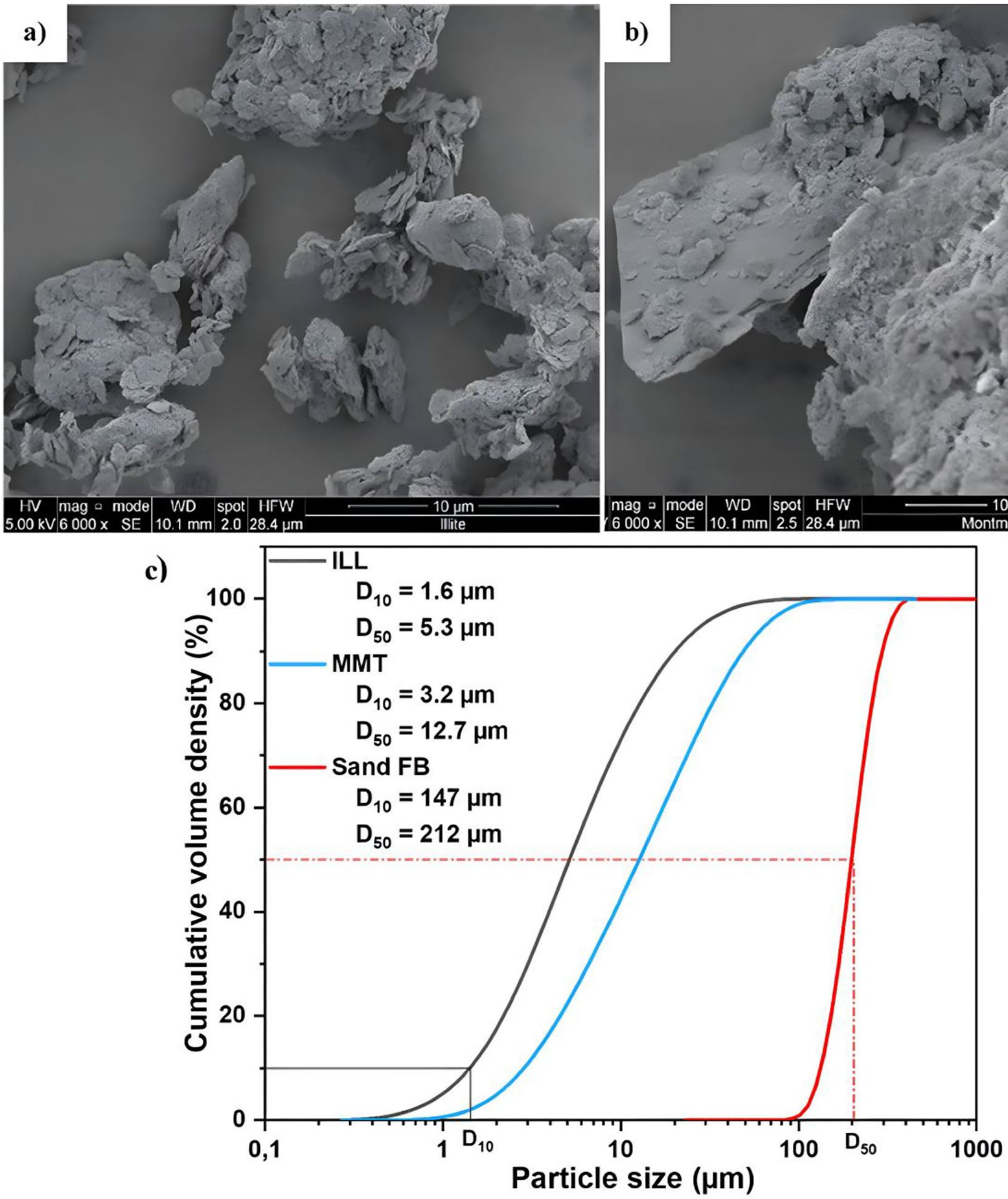

Figure 1. Scanning Electron Microscopy images showing aggregated platy particles of (a) ILL and (b) MMT. (c). Particle Size Distribution of Fontainebleau sand and the clay-rich matrices (ILL and MMT) determined by a Malvern Mastersizer 3,000 laser. (a) D_{10} and D_{50} (D_{mean}) are grain sizes below which 10% and 50% of all particles are found, respectively.

latter was used when it was necessary to recover the hydrate-bearing core for visual inspection. The matrix was unconsolidated and therefore subjected to very low or practically no effective stress (self-weight).

Prior to any experiment, the apparatus was vacuumed by applying pressure of about 10^{-6} MPa in order to remove any residual air pockets from the matrix. Water was injected at 293.15 K with constant flowrate (2.5 and 0.5 g min^{-1} for pure sand and clay-rich matrices, respectively) in the center of the upper flange of the cell for optimal distribution in the matrix. The system was then left at 293.15 K for 24 hr to ensure no further gravitational water movement in the matrix.

Prior to gas injection, cell temperature was set at 277 K before gas supply. Once thermal stability was reached (4 hr minimum), methane was injected through the bottom of the cell (Figure 2) at a constant flowrate of

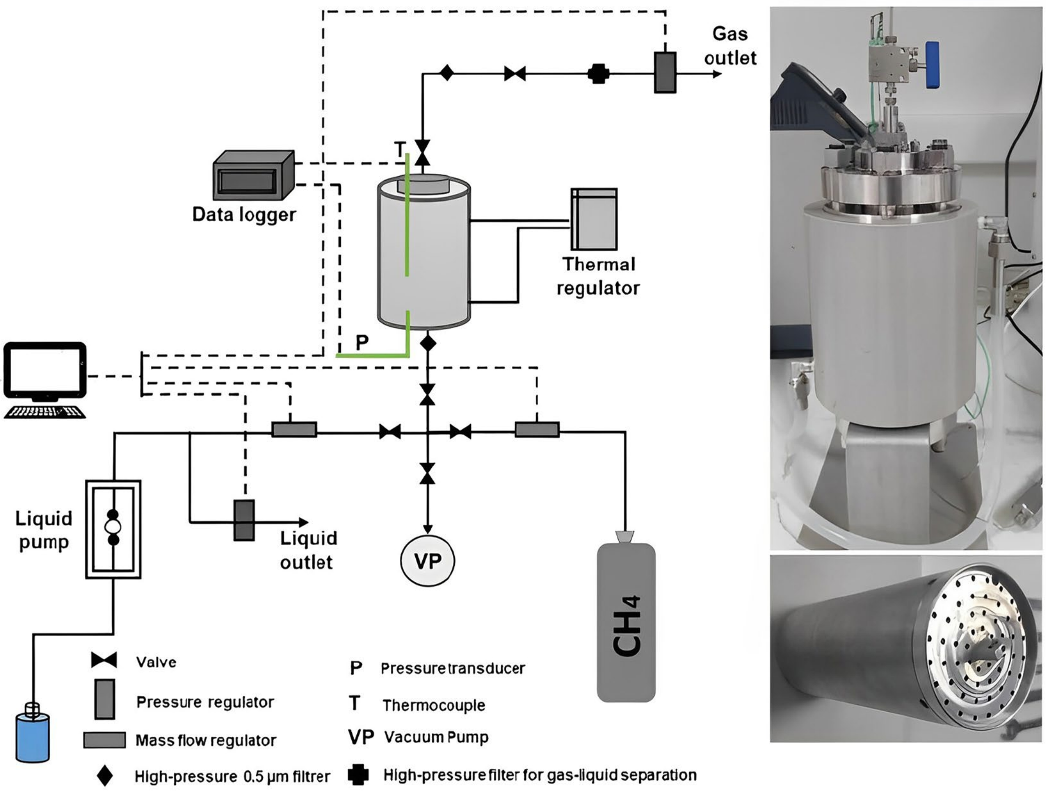

Figure 2. Schematic diagram of the apparatus used to synthesize hydrate-bearing cores. The images to the left depict the high-pressure cell (top) and the aluminum cell (bottom).

57 mLn min^{-1}, until the system reached the gas cylinder pressure (~11 MPa). During methane injection, the temperature, as well as the upstream and downstream pressures of the cell, were recorded every 10 s. Hydrate formation was detected from a pressure drop (illustrated by a change in pressure slope when monitoring the evolution of pressure as a function of time) associated with a sudden increase in temperature due to the exothermic nature of hydrate formation (Figure 3). The gas injection was stopped when the pressure remained stable for at least 15 hr to ensure completion of hydrate formation.

2.2.3. Design the Experiments

Three series of experiments were performed:

1. The first series was dedicated to the investigation of the effect of clay content on hydrate formation in porous media. Experiments were carried out with partially saturated sand-clay mixtures with various clay content and at a constant volume of water (V_W). The latter was calculated as follows:

$$V_w = S_w \times V_V \tag{1}$$

$$V_V = V_{Cell} - V_S - 2 \times V_{ps} \tag{2}$$

Where V_{cell} (mL) is the aluminum cell effective volume, the volume of voids V_V (mL), V_{ps} (mL) is the volume of the porous stone, and V_S (mL) is the sand volume computed from the sand grain density ($\rho_S = 2.65$ g/cm^3).

Equation 2 is only used to determine the volume of voids in sand. Since sand and clay-rich matrices do not have the same density and porosity, water saturation in the presence of clay was calculated from their estimated porosity (n), using geometric soil parameters (Holtz et al., 2011):

$$e \times S_w = G_S \times \omega \tag{3}$$

Table 2
Mineralogical Composition and Properties of the Different Clay Matrix/Sand Mixtures Used for the Experiments

	Mixtures		Mineralogy				Hydraulic conductivity
	Clay matrix	Sand FB (%)	Clay (%)	Quartz (%)	Calcite (%)	Porosity	K (m s^{-1})[a]
Sand	0	100	–	100	–	0.42	2×10^{-4}
ILL/Sand	17.9	82.1	10.0	87.3	2.3	0.47	4.80×10^{-9}
	35.7	64.3	20.0	74.6	4.6	0.52	4.36×10^{-10}
	71.4	28.6	40.0	49.3	9.3	0.58	2.37×10^{-10}
	100	0.0	~60	29.0	13.0	0.63	2.23×10^{-10}
MMT/Sand	15.2	84.8	10.0	87.6	–	0.48	2.08×10^{-8}
	90.9	9.1	~60	25.5	–	0.74	1.08×10^{-8}
	ILL (%)	MMT (%)	Illite (%)[b]	Smectite (%)[b]	Kaolinite (%)[b]		
MMT/ILL	90.0	10.0	70.8	10.9	15.5	0.63	–
	70.0	30.0	58.4	26.7	12.5	0.66	–
	47.0	53.0	44.1	44.9	9.1	0.69	–

[a]For sand, K is obtained by Hazen's equation: K = CH × D102 (Holtz et al., 2011). For clay matrix/sand mixtures, values were obtained by oedometer tests conducted in the laboratory according to the standard method D5856-15 of ASTM International (ASTM, 2007). [b]The proportions given here represent the resulting clay fraction mineralogy calculated from the composition of the original materials (Table 1).

$$e = \frac{n}{1 - n} \tag{4}$$

Porosity is derived from Equations 3 and 4:

$$n = \frac{\omega}{\omega + \frac{1}{G_S}} \text{ for } S_w = 100\% \tag{5}$$

Where e is the void ratio, G_S (2.66) is the specific gravity of soil solids and ω (%) is the water content, obtained by the ratio between the pore water weight and the solid grains weight. A detailed description of this procedure is given in the Supporting Information S1. Calculated porosity values are reported in Table 2. These values are used to obtain the volume of voids, which then allows to calculate water saturation using Equation 1.

2. The second set of experiments aimed to jointly examine the effect of water saturation and clay type on hydrate formation. They were performed only with the aforementioned clay matrices, at ~60% of clay (Table 2), but with different water saturation varying from 40% to 82% for ILL and from 35% to 100% for the MMT-rich matrix.
3. The purpose of the third set was to study the kinetic behavior of hydrates in the presence of different mixtures of the two types of clay. Experiments were performed at 75% water saturation with three MMT/ILL mixtures with mass ratio of 10/90, 30/70, and 47/53 (Table 2), respectively.

After each experiment, the cell was quickly depressurized before recovering the hydrate core. The core was cut longitudinally immediately after recovery for hydrate morphology observation, and then stored in liquid nitrogen at 77 K. Selected cross sub-sections were made later to collect specific samples for micro-Raman spectroscopy analysis.

2.3. Recovery and Sampling of Natural Gas Hydrate From the Western Black Sea

A 6-m-long hydrate-bearing core, labeled GAS2-CS05, was recovered at 734 m water depth and ~9°C during the Ghass2 Cruise (2021) in the Romanian sector of the Western Black Sea. The core was cut into sections of 1 m in length and opened lengthwise to collect hydrate specimens with a sampling resolution of ~10–30 cm (Table 3). The samples were preserved in liquid nitrogen for future analysis by micro-Raman Spectroscopy. Sediment samples were also collected near the hydrates within the core for subsequent mineralogy analysis and particle size distribution (Table 3). Overall, the sediment is composed on average of ~60% clay, ~23% quartz, and ~8.5% calcite. However, clay mineralogy varies with depth, with the upper 2.4 m dominated by illite (~62%) and a smectite-rich lower part (~53%).

2.4. Micro-Raman Spectroscopy Analysis

2.4.1. Apparatus and Experimental Procedure

Micro-Raman analyses were performed using a Labram HR Evolution spectrometer (Horiba, Jobin Yvon, France) coupled with a confocal microscope allowing to accurately investigate a specimen over a micrometric area. A 405 nm wavelength solid laser produces the excitation source and the beam is focused on the sample thanks to a ×50 long working distance objective. The confocal pinhole is set to 300 µm and the collected Raman

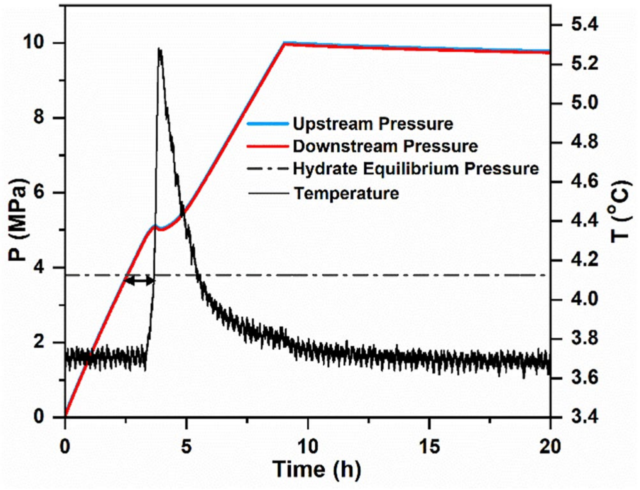

Figure 3. Example of typical pressure and temperature profiles during hydrate formation. (←→) Represents induction time. Upstream and downstream pressures are measured at the bottom and top of the core, respectively. Hydrate equilibrium pressure in bulk phase at 277 K is 3.8 (dashed black line) (Sloan & Koh, 2007).

scattering was dispersed by a holographic grating of 1,800 grooves/mm and was analyzed by a Peltier-cooled charge-coupled device (CCD detector (Andor, Belfast, UK). The spectral resolution (full-width at half-maxima) was 2.5 cm^{-1} with a CCD spectral pixel size of 1 cm^{-1}. Prior to the analysis of hydrate samples, the wavenumber of the spectrometer was calibrated with the 520.7 cm^{-1} mode of a silicon sample.

The hydrate samples are first cold-crushed (under inert atmosphere in liquid nitrogen) to avoid condensation deposits on the hydrate grains. These powdered samples are then cold-transferred onto a Linkam stage (THMS600, Linkam Scientific Instruments Ltd., UK). To prevent hydrate dissociation, the temperature of the cell is maintained at 150 K. In order to study the variability of cage occupancy, 121 Raman spectra were collected over a probed area for each synthetic hydrate sample and 221 spectra were collected for each natural specimen from the Black Sea core. Raman spectra were recorded in a range from 150 to 3,880 cm^{-1} and with an acquisition time of 40 s in two accumulations.

2.4.2. Calculation of Cage Occupancy and Gas Storage Capacity

Cage occupancy (θ) can be obtained from the integrated intensities of the Raman spectral bands of methane hydrate. These well-known peaks at 2,904 and 2,915 cm^{-1} (Figure 8) correspond to the C–H symmetric stretching vibrational frequencies of CH_4 (ν_1 mode) trapped in large (LC) and SC, respectively (Sum et al., 1997; Tulk et al., 2006). Since the number of large cages is three times that of SC in the SI hydrate structure, the relative cage occupancy of large to SC is expressed as follows:

$$\frac{\theta_{\mathrm{LC}}}{\theta_{\mathrm{SC}}} = \frac{A_{\mathrm{LC}}}{3A_{\mathrm{SC}}} \times \frac{\sigma_{\mathrm{SC}}}{\sigma_{\mathrm{LC}}} \quad (6)$$

Where θ_{LC} and θ_{SC} are the absolute cage occupancies in large and SC, respectively; A_{LC} and A_{SC} are the Raman peak integrated intensities (areas) of the large and SC, respectively. These areas are determined by peak deconvolution using the Gauss/Lorentz function after a suitable baseline correction with the software Labspec 5. σ represents the Raman scattering cross section for each cage and $\sigma_{\mathrm{LC}}/\sigma_{\mathrm{SC}}$ is 0.977 for CH_4 hydrate (Qin & Kuhs, 2013).

To calculate absolute cage occupancies, the relative cage occupancy obtained from micro-Raman measurements is coupled with the well-known Van der Waals and Platteeuw thermodynamic theory (Waals & Platteeuw, 1958), expressing the chemical potential of water in the SI hydrate:

$$\mu_{\mathrm{w}}(h) - \mu_{\mathrm{w}}(h_0) = -\frac{\mathrm{RT}}{23} 3\ln(1-\theta_{\mathrm{LC}}) + \ln(1-\theta_{\mathrm{SC}}) \quad (7)$$

Table 3
Hydrates Samples Depth, Average Mineralogy, and Mean Particle Size of Their Associated Sediments

Hydrates samples	Associated sediments		
Depth (m)	Global mineralogy	Clay mineralogy	D_{50} (μm)
0.39–2.40	Clays (~65%)	Illite (~62%)	~4.5
	Quartz (~19%)	Smectite (~11%)	
	Calcite (~7%)	Kaolinite (~20%)	
		Chlorite (~7%)	
2.50–5.80	Clays (~57%)	Illite (~28%)	~27.6
	Quartz (~26.5%)	Smectite (~53%)	
	Calcite (~5%)	Kaolinite (~14%)	
		Chlorite (~5%)	

Where $\mu_{\mathrm{w}}(h)$ is the chemical potential of water in a hypothetical empty lattice, and $\mu_{\mathrm{w}}(h_0)$ is the chemical potential of water in a reference state. In the equilibrium state:

$$\mu_{\mathrm{w}}(h) - \mu_{\mathrm{w}}(h_0) = \Delta\mu_{\mathrm{w}}{}^{0} \quad (8)$$

And $\Delta\mu_{\mathrm{w}}{}^{0}$ is the difference between the chemical potential of water in the empty gas-hydrate lattice and the stable-ice lattice, whose commonly used value is 1297 J mol^{-1} (Davidson et al., 1986). The Van der Waals and Platteeuw theory assumes that the free energy of the hydrate is independent of cavity occupation, that one hydrate cavity contains only one guest molecule, and that the interactions between guest molecules are negligible.

The absolute occupancies of the cages are obtained by combining Equations 6 and 7. Thus, the gas storage capacity (GSC in m^3) or EF, which corresponds to the volume of methane that can be released by the dissociation of a unit volume of hydrate in standard conditions (0°C and 1 atm), is calculated as defined in Merey and Sinayuc (Merey & Sinayuc, 2016):

$$\mathrm{GSC} = \mathrm{EF} = \frac{M_{\mathrm{CH_4}}}{M_{\mathrm{CH_4}} + \mathrm{N} \times \mathrm{M_{H_2O}}} \times \frac{\rho_{\mathrm{H}} \times V_{\mathrm{H}}}{\rho_{\mathrm{CH_4}}} \tag{9}$$

And

$$N = \frac{23}{3\theta_{\mathrm{LC}} + \theta_{\mathrm{SC}}} \tag{10}$$

N is the hydration number of CH_4 hydrate, M_{CH4} and M_{H2O} (g mol^{-1}) are the molar weights of CH_4 and H_2O, respectively; V_H is the unit hydrate volume (1 m^3); ρ_H and ρ_{CH4} are the densities of CH_4 hydrate (910 kg m^{-3}) CH_4 gas (0.717935 kg m^{-3}), respectively, in standard conditions.

3. Results and Discussion

3.1. Hydrate Morphology and Structural Load Carrying Fraction

Both the hydrate-bearing cores synthesized from the series of laboratory experiments in the different matrices composed of pure sand, ILL/sand, MMT/sand, MMT/ILL mixtures with different clay contents (10%–∼60%) and the natural hydrate samples, were visually inspected in order to describe the hydrate morphology (Holland et al., 2008; Terzariol et al., 2020, 2021).

Figure 4 shows selected photographic images of the morphology of hydrates formed in different matrices. Hydrates in the sandy matrix are widely distributed along the cores. Cross sections (Figure 4a) show that hydrates are concentrated in the central part of the core. These areas of the cores exhibited a more pronounced resistance to splitting. Similar experimental observations of hydrates appearing as cement between sand grains were made by Ruffine (2015) and Klapproth et al. (2006). In clay/sand matrices with clay content of 10% (Figures 4b and 4c), morphology is similar to that observed in sand, but the distribution is more heterogeneous. In the 17.9% ILL/82.1% sand mixture, hydrates are more concentrated in the lower part of the core (Figure 4b), whereas they are more widely distributed along the core when the clay used is MMT (white parts, Figure 4c).

A different morphology is observed in the 35.7% ILL/64.4% sand mixtures (Figure 4d). The hydrates exhibit a grain-displacive behavior and are localized in the central and lower parts of the cores. They are massive and are arranged as veins with thickness varying from 1 to 3 mm. In the 71.4% ILL/28.6% sand matrix, hydrates also displace particles to form dispersed nodules (Figure 4e). They form a network of interconnected fine millimeter-thick veins (Figure 4e). This morphology, resulting from grain displacement, is increasingly pronounced in the more enriched clayey matrix and in the MMT/ILL mixtures, with the thickest hydrate veins observed in our experiments (Figures 4f and 4g). The photographic images of the Black Sea natural hydrates show that the morphologies observed on our clay-rich synthetic hydrates are consistent with natural hydrate-bearing sediments. Hydrates fill parallel fractures in the Black Sea clayey sediments (Figures 4g and 4i).

Sediment properties control hydrate morphology. A pore-invasive and grain-displacive pore habit can be anticipated from the ratio of pore-throat capillarity Δu and effective stress σ' (Dai et al., 2012; Terzariol et al., 2020, 2021). Capillary pressure is estimated by:

$$\Delta u = \frac{4T_S}{r} \tag{11}$$

Where T_s (∼0.039 N/m) is methane hydrate/water interfacial tension; r is the mean pore size and can be approximated for sand by $(\sqrt{2}-1)D_{10}$. In the case of clayey matrices (ILL and MMT), this pore size can be estimated from specific surface (S_s), mineral density (ρ_m), and void (e) (equations and explanation in Terzariol et al. (2021)):

$$\mathrm{d_p} = \frac{2e}{\mathrm{S_s}\rho_{\mathrm{m}}} \tag{12}$$

A first-degree approximation of the capillarity in our test sediments, shows that $\Delta u = 3$ kPa in sand FB, while in ILL and MMT, this value reaches 9 and 12 MPa respectively. Thus, it can be expected that sand FB might form pore-filling hydrate even in the absence of applied vertical loads. On the other hand, ILL and MMT will favor grain-displacive hydrate formation as observed in our experiments.

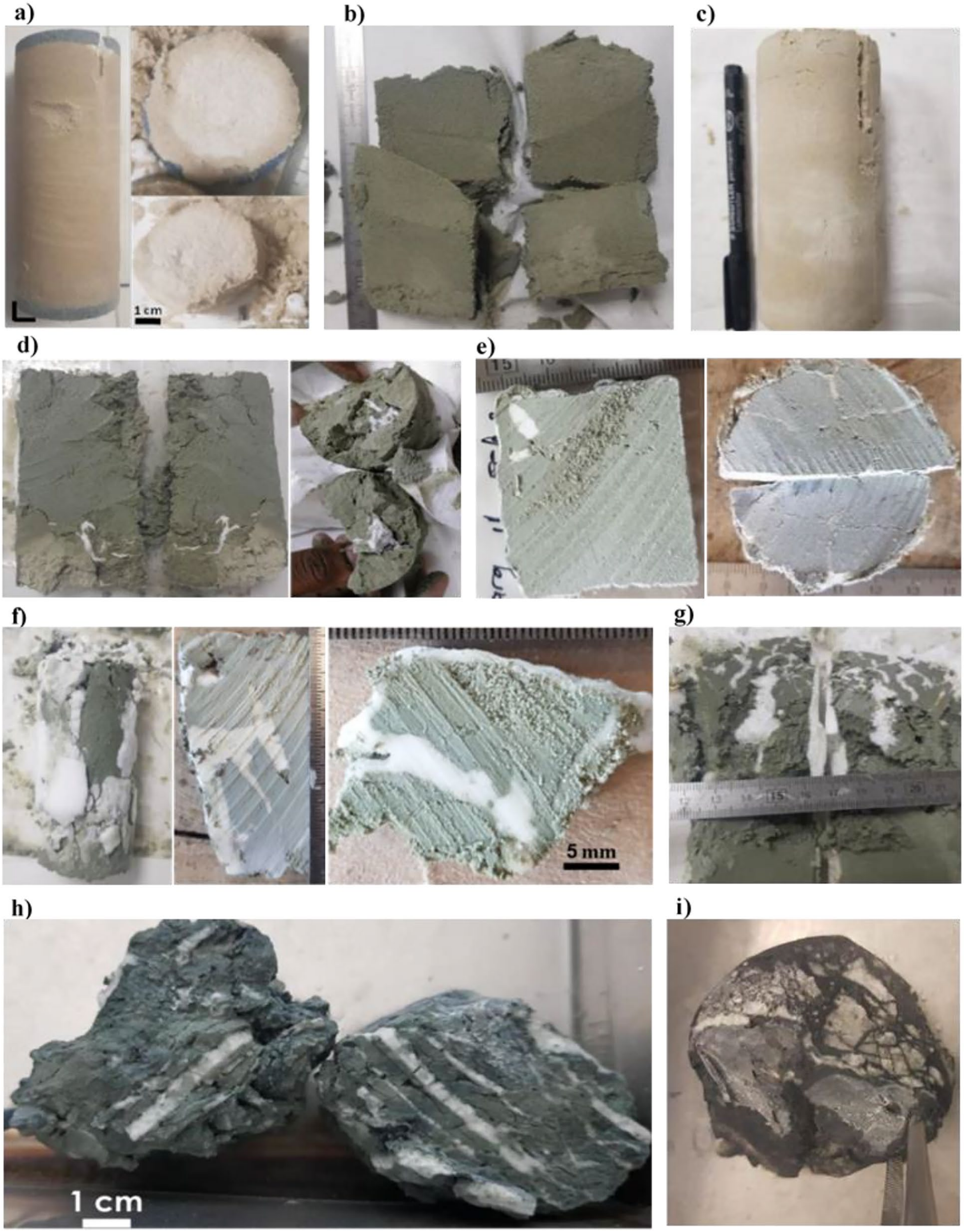

Figure 4. Photographic images showing the morphology of synthetic hydrate-bearing sediment (a–g) and natural specimens (h, j): (a) Disseminated hydrates in sand. (b, c) Disseminated hydrates in sand. (b, c) Disseminated hydrates in clay matrix: (b) 17.9% ILL/82.1% sable, (c) 15.2% MMT/84.8% sand. (d) Hydrate veins and nodules in clay matrix (35.7% ILL/64.3% sand). (e) Nodules and vein network in clay (71.4% ILL/28.6% sand). (f) Thick veins and hydrates surrounding the matrix (100% ILL). (g) Network of hydrate veins of variable thickness in a MMT/ILL matrix. (h) Natural sample collected at 5.35 mbsf showing hydrate-filling fractures. (i) Massive hydrate sample collected at 3.2 mbsf in the in the Romanian sector of the Western Black Sea.

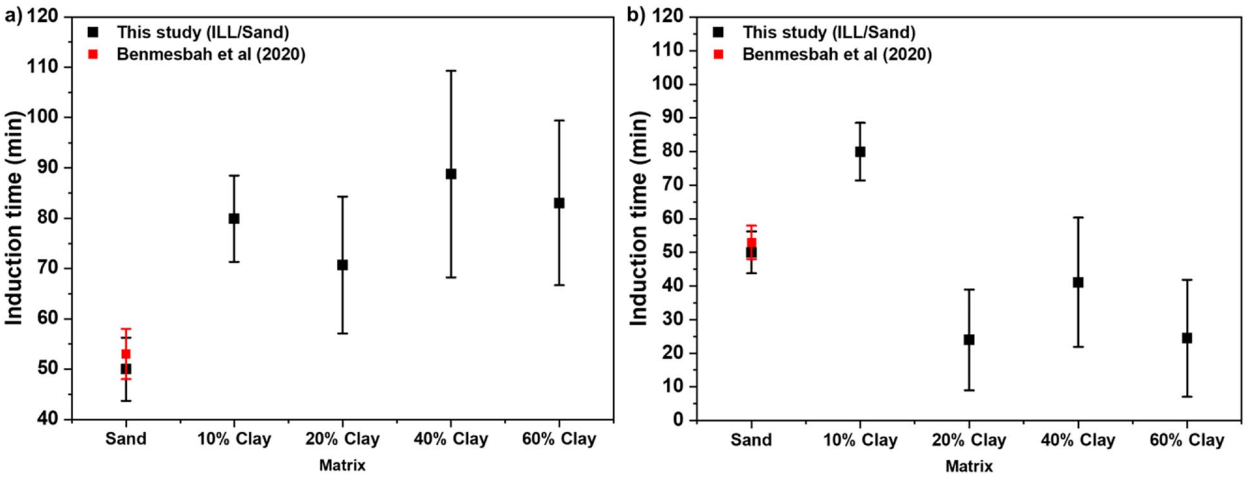

Figure 5. Average values of induction time for hydrate formation in matrices with different clay content and at constant water volume (not constant water saturation). (a) Measured induction time from bulk hydrate equilibrium pressure. (b) Corrected induction from capillarity effect. Bars represent the standard deviation. Experiments of Benmesbah et al. (2020) were carried out in the same conditions as the present study (sandy matrix, and same water saturation and methane injection flowrate).

In the case of a fines (i.e., particle size ≤74 μm)/coarse mix sample, we needed to determine which sediment fraction carries the mechanical load. The ILL and MMT matrices are both fines since they have $D_{99.85}$ and D_{97} smaller than 74 μm (Figure 1c). In other words, the proportion of either the ILL or MMT matrix in a mixture corresponds to the fines content. The Revised Soil Classification System (RSCS) (Park & Santamarina, 2017) allows us to estimate the fines fraction thresholds (FF) from compacity (for sands) and effective stress dependent void ratios (for fines). An ILL/sand FB and MMT/sand FB mixtures show a mechanical transition zone of FF = 15%–29% and 8%–20%, respectively, displaying good agreement with the fine content at which the change in morphology occurs in our synthesized samples. Regarding fluid flow, these thresholds are FF = 8% and 2.5% for ILL/sand and MMT/sand, respectively.

3.2. Kinetics of Hydrate Formation

3.2.1. Influence of Clay Content on Induction Time

The induction time is defined as being the elapsed time between the equilibrium pressure of methane hydrate at experiment temperature and the pressure drop associated with the onset of hydrate formation (Figure 3). Figure 5a summarize the measured induction times for the first series of experiments performed at constant injected water volume in sand and clay/sand mixtures (experiments 1_1 to 5_5 in Table 4). The average induction time for hydrate formation within the sand is 50 ± 6 min, which is close to the value of 53 ± 5 min obtained by Benmesbah et al. (2020) in a previous study using the same apparatus and operating conditions.

As shown in Figure 5a, once clay was added to sand, even in a small amount, the induction time significantly shifted to higher values. The addition of 10% of clay to a sandy matrix increases the induction time from 50 min (without any clay) to 80 ± 8 min, for example, an increase of ~60%. Our experiments indicate that the variation of induction time is relatively small when varying the amount of clay in the ILL/sand matrix. Despite data scattering (Table 4), likely related to the stochastic nature of hydrate nucleation (Bagherzadeh et al., 2011; Linga et al., 2009; Mekala et al., 2014), the values of induction time remains relatively constant for matrices with 20%, 40%, and ~60% of clay, with values of 71 ± 13, 89 ± 20, and 83 ± 16 min, respectively. Therefore, our results suggest that clay acts as a kinetic inhibitor for this VW. This is in agreement with previous conclusions of Zhang et al. (2017) who also show that the addition of 10 wt% of bentonite clay to sand, at 55% of water saturation, significantly increases the induction time, which then remains almost unchanged even for clay content up to 30 wt %.

It is well known that gas flow is a key factor controlling hydrate formation in sediment (Xu & Ruppel, 1999; You et al., 2019). As mentioned by Park and Santamarina (Park & Santamarina, 2017), the presence of fines, at even a low content, is enough to drastically affect fluid flow in sand/clay mixtures. In the present work, we have estimated this fines fraction FF = 8% for the ILL/sand mixtures. Thus, the addition of ILL ($D_{99.7} < 74$ μm) fills the voids between sand particles, leading to a reduction in matrix permeability, and therefore strongly hindering gas migration to the hydrate formation front. This is partially supported by hydraulic conductivity (K),

Table 4
Summary of Measured Kinetic Parameters From Differents Series of Hydrate Formation Experiments

Mixtures	Experiments	Clay content (ratio clay matrix/sand)	Water saturation (%)	Measured induction time (min)	Pressure at the onset of hydrate formation (MPa)	Amplitude of the thermal anomalies ΔT (°C)	Load carrying fraction	Void ratio for fines at low effective stress	Pore size diameter (µm)	Corrected induction time from capillarity
Sand	1_1	0% clay (0/100)	56.0	55.8	5.10	1.10	Sand	N/A	60.8	55,8
	1_2		56.7	50.5	4.78	0.81	Sand	N/A	60.8	50,5
	1_3		56.0	43.3	4.71	0.73	Sand	N/A	60.8	43,3
ILL/Sand	2_1	10% clay (17.9/82.1)	52.0	83.3	5.22	1.66	Sand	N/A	60.8	83,3
	2_2		52.4	70.2	5.12	1.58	Sand	N/A	60.8	70,2
	2_3		52.4	86.3	5.71	1.66	Sand	N/A	60.8	86,3
	3_1	20% clay (35.7/63.4)	49.0	81.3	5.50	0.61	ILL	1.52	0.017	34,0
	3_2		49.0	75.3	5.34	1.69	ILL	1.52	0.017	29,3
	3_3		49.0	55.3	4.82	1.42	ILL	1.52	0.017	6,0
	4_1	40% clay (71.4/28.6)	45.0	72.5	4.47	0.44	ILL	1.52	0.017	–
	4_2		45.0	82.0	5.22	1.16	ILL	1.52	0.017	27,5
	4_3		45.0	111.8	5.63	1.27	ILL	1.52	0.017	54,7
	5_1	60% clay (100/0)	41.3	99.7	5.45	0.63	ILL	1.52	0.017	42,7
	5_2		41.2	95.2	5.38	1.36	ILL	1.52	0.017	39,0
	5_3		41.0	65.0	4.87	1.25	ILL	1.52	0.017	7,2
	5_4		41.0	66.3	4.81	1.53	ILL	1.52	0.017	5,5
	5_5		41.0	88.4	5.20	1.13	ILL	1.52	0.017	28,2
	6_1	60% clay (100/0)	55.0	56.7	4.84	0.54	ILL	1.52	0.017	5,3
	6_2		55.0	53.0	4.82	0.48	ILL	1.52	0.017	3,7
	6_3		55.0	67.2	4.98	0.57	ILL	1.52	0.017	13,0
	7_1	60% clay (100/0)	62.0	44.0	4.57	0.40	ILL	1.52	0.017	–
	7_2		62.0	60.0	4.91	0.91	ILL	1.52	0.017	9,7
	7_3		62.0	39.0	4.51	0.46	ILL	1.52	0.017	–
	8_1	60% clay (100/0)	82.0	59.7	4.98	0.31	ILL	1.52	0.017	11,7
	8_2		82.0	52.2	4.91	0.30	ILL	1.52	0.017	7,7
	8_3		82.0	52.2	4.92	0.67	ILL	1.52	0.017	9,0

Table 4
Continued

Mixtures	Experiments	Clay content (ratio clay matrix/sand)	Water saturation (%)	Measured induction time (min)	Pressure at the onset of hydrate formation (MPa)	Amplitude of the thermal anomalies ΔT (°C)	Load carrying fraction	Void ratio for fines at low effective stress	Pore size diameter (µm)	Corrected induction time from capillarity
MMT/Sand	9	10% clay (15.2/84.8)	52.0	90.0	5.87	4.09	Sand	N/A	60.8	90,0
	10	60% clay (91/9)	36.0	125.2	5.93	3.01	MMT	4.04	0.013	51,2
	11_1	60% clay (91/9)	55.0	132.5	6.22	4.11	MMT	4.04	0.013	65,3
	11_2		55.0	100.0	5.67	3.75	MMT	4.04	0.013	34,0
	12_1	60% clay (91/9)	75.5	60.5	5.13	2.40	MMT	4.04	0.013	5,5
	12_2		75.0	83.7	5.68	2.87	MMT	4.04	0.013	29,2
	13	60% clay (91/9)	100	38.7	4.95	0.35	MMT	4.04	0.013	–
	14	~60% (10 MMT/90 ILL)	75.0	89.2	5.83	0.20	ILL	1.52	0.017	52,0
MMT/ILL	15_1	~60% clay (30 MMT/70 ILL)	75.0	85.1	5.67	0.18	ILL	1.52	0.017	40,8
	15_2		75.0	92.7	5.76	0.16	ILL	1.52	0.017	50,0
	16_1	~60% clay (53 MMT/47 ILL)	75.0	126.0	6.83	0.22	MMT	4.04	0.013	69,2
	16_2		75.0	135.0	6.73	0.35	MMT	4.04	0.013	79,7

proportional to the intrinsic permeability of the matrices used here. K for sand is 2×10^{-4} m s^{-1}, whereas the values for the mixtures ILL/sand with 10%, 20%, 40%, and ~60% clay are 4.80×10^{-9}, 4.36×10^{-10}, 2.37×10^{-10}, and 2.23×10^{-10} m s^{-1}, respectively. A difference of five orders of magnitude is noted between the hydraulic conductivity of the sandy matrix and the mixture with 10% clay (17.9% ILL). Considering our gas injection procedure, this large difference could be one plausible explanation for the longer time observed for hydrate formation in 10% clay matrix. Such behavior may explain the fact that the induction time remains almost constant for the matrices ILL/sand, irrespective of the clay content, since the values of their permeabilities are very close.

To take account for capillarity effect inherently related to small pore size in clayey sediments, we corrected the induction time discussed above and measured based on the bulk hydrate equilibrium pressure. This correction requires to determine the methane hydrate equilibrium pressures associated with the different mixtures porous media (sand, ILL, MMT, and their different mixtures) at the experimental temperature (~277 K). In fact, the conclusions of several studies have shown the thermodynamic inhibiting effect of small pore size, which shifts the hydrate phase boundary of hydrates toward lower temperatures and/or higher pressures (Handa & Stupin, 1992; Østergaard et al., 2002; Uchida et al., 2002). The temperature depression (ΔT_{pore}) related to this effect is calculated using Equation 5 in Lee et al. (2008) and first introduced by Clennell et al. (1999):

$$\Delta T_{\text{pore}} = \frac{2\Upsilon_{\text{Hw}} T_{\text{bulk}} \cos\theta}{\rho_{\text{H}} \Delta H r} \tag{13}$$

Where Υ_{Hw} (27 mJ m^{-2}) (Clennell et al., 1999) is the hydrate-water interfacial tension, T_{bulk} (K) is the methane hydrate equilibrium temperature in bulk phase, θ the contact angle between the pore wall and hydrate, ρ_{H} (kg m^{-3}) is the hydrate mass density, ΔH (kJ kg^{-1}) the heat of hydrate dissociation, and r is the pore size of the sediment. Due to the lack of pore size distribution, this latter parameter were estimated is this study for each mixture from the load fraction carrying (RSCS) as suggested in Terzariol et al. (2020). As explained in Section 3.1, the operation consists in defining which fraction of a clay matrix/sand matrix mixture controls its mechanical behavior. The results of the load carrying fraction reported in Table 4, were obtained from the fines fraction thresholds previously calculated: 29% at low effective stress for ILL/sand and MMT/sand, respectively. As a result, the mixture 17.9 ILL/82.1 sand (with 10% clay) for example, is sand-controlled while the others are ILL-controlled. The mean pore diameters of these load carrying fractions sand, ILL and MMT are 60.8, 0.017, and 0.013 µm, respectively.

The application of Equation 13 to these pore sizes allowed to determine the hydrate equilibrium pressures at the experimental temperature (~277K), whose values are ~38 bar (similar to the bulk phase) for sand, ~4.8 for ILL and ~5.1 MPa for MMT. Based on the changed equilibrium conditions, the corrected induction times in mixtures affected by capillarity were found to be lower, than those previously obtained by considering a bulk equilibrium pressure of methane hydrate. As seen in Table 4 and Figure 5b, the trends of the evolution of the induction time in the ILL/sand are modified. Values remained unchanged for sand and 10% clay matrix where hydrate formation is not subjected to the capillarity pressure because of the large pore size (60.8 µm). Thus, it can still be observed that the induction time increases with the addition of 10% clay to sand. However, it decreases when the clay

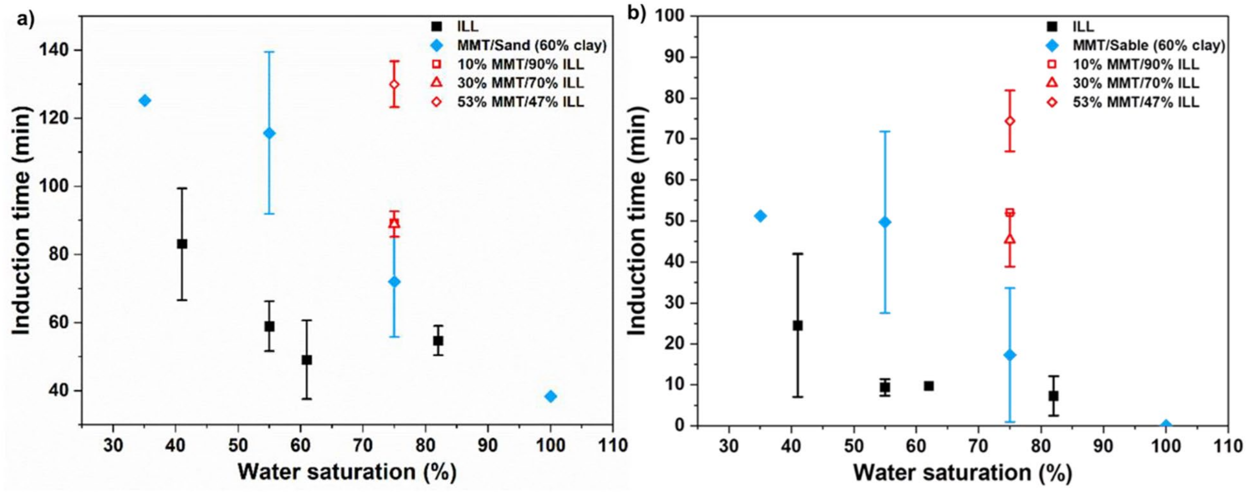

Figure 6. Induction time as a function of the initial water saturation in illite and montmorillonite-rich clay. (a) Measured induction time from bulk hydrate equilibrium pressure. (b) Corrected induction from capillarity effect. There is no addition of sand to the MMT/ILL matrices. Note that the experiments at 41% water saturation for ILL are also represented in Figure 5 at 60% clay for a constant amount of water.

content reaches 20% (i.e., when the load-carrying fraction is the clay matrix ILL) and remains relatively constant with further increase of the clay content. Indeed, applying the capillarity correction shifts the equilibrium pressure to higher values (from ∼3.8 in bulk phase to 4.8 MPa). The latter becomes located closer to the hydrate formation incipient pressure (e.g., the pressure drop) that occurs well after reaching the equilibrium pressure of methane hydrate within the cell. Thus, mechanically, the induction time is shortened. However, this result with the increase in clay content is unexpected since capillarity should inhibit hydrate formation. Nevertheless, this trend could be explained by the small size of clay particles and their high specific surface area compared to sand. As emphasized in previous studies, this specific surface area of small grains provides a greater number of hydrate nucleation sites and thus reduce the induction time (Chong et al., 2016; Heeschen et al., 2016; Mekala et al., 2014).

These results are not in agreement with those of Zeng et al. (2022) and Zhang et al. (2017) who rather observed an increase in induction time in a sand-clay mixture with increasing clay content. However, none of these studies take into account the effect of capillary pressure on hydrate equilibrium conditions in the determination of induction time. All these elements discussed highlight the complexity of hydrate formation mechanisms in the presence of clay, including gas transport, the effect of grain size and capillarity driven by small pores.

3.2.2. Influence of the Initial Water Saturation and Nature of Clay on Hydrate Formation Kinetics in Clay-Rich Matrices

This section is dedicated to the results obtained after the series of experiments (2) and (3) in the experimental section (experiments 5_1 to 8_3 and 10 to 16_2 in Table 4). Figures 6a and 6b show respectively the measured and corrected (from capillarity) induction time of hydrate formation in clay-rich matrices (ILL and MMT) at different initial water saturations. It can be observed that the trends of the recalculated induction times are broadly the same as those measured according to bulk hydrate equilibrium conditions. However, previous work showed that capillary-induced depressions in equilibrium temperatures (ΔT_{pore}) is reduced with increasing water saturation (Uchida et al., 2004; Vavra et al., 1992). Therefore, it become less relevant to apply the correction only based on the theoretical pore diameter explained in Section 3.2.1. From our data set, it seems difficult to take quantitatively into account the variation of the capillary pressure with the water saturation. The following discussion, regarding the evolution of the induction as function of water saturation in ILL and MMT, is based on the initial measured values (Figure 6a), although it remains valid for Figure 6b.

The experiments performed with the ILL matrix show that induction time decreases significantly from 83 ± 16 to 49 ± 11 min when water saturation increases from 40% to ∼62% and then remains relatively steady with a further increase in water saturation; whereas a continuous decrease in induction is observed for experiments performed in the MMT-rich matrix (Figure 6b). Induction time is reduced by a factor of 3.2 when water saturation increases

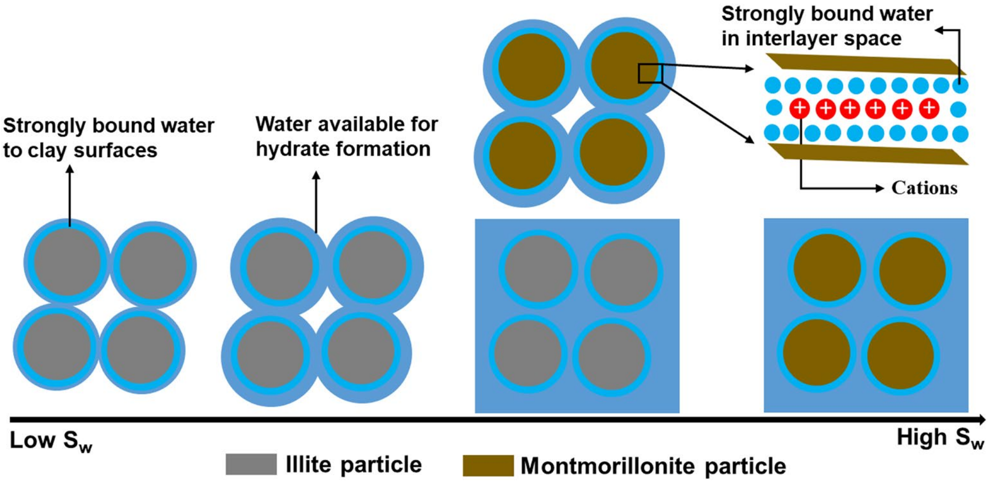

Figure 7. Schematic representation of water distribution in illite and montmorillonite as a function of water saturation.

from 35% to 100%. It is well known that clays have a high water adsorption capacity owing to their high specific surface area (Kumari & Mohan, 2021; Martin, 1960). In addition, clay minerals have a strong adsorption regime at low water content (Hatch et al., 2012; Schuttlefield et al., 2007), which consequently reduces the amount of water available for gas/water contact at low water saturation. Additionally, the inherent capillarity pressure associated to the small pores of ILL (0.017) and MMT (0.013 μm) is more significant at low water saturation and thus affecting the hydrate formation behavior.

Furthermore, the trends observed in Figure 6 indicate that hydrate formation occurs faster in ILL than in MMT-rich matrix for low to medium water saturation levels ($S_w \leq 55\%$). Thus, the average induction time is almost twice higher for hydrate formation in montmorillonite than in illite for a saturation of 55%. This could be attributed to the different capillarity pressures and different water absorption capacities and mechanisms related to the different properties and mineral structures of these two types of clay. First, in agreement with its larger specific surface (240.8 m^2/g, Table 1), MMT has a higher adsorption capacity than ILL (66.4 m^2/g). In addition, with its structural ability to swell, water uptake in montmorillonite is done by adsorption not only on the external surfaces of the clay particles but also and especially in interlayer spaces with hydration of exchangeable cations (Cases et al., 1992), whereas adsorption in illite only occurs on external surfaces (Figure 7) (Dettmann, 1958). These additional sites for bound-water in montmorillonite strongly affect water availability and could therefore delay hydrate formation mainly at low to medium water saturation. As water content increases, water fills the pores of the matrix (Cases et al., 1992; Hatch et al., 2012; H. Wang et al., 2020) and capillarity decreases (Vavra et al., 1992), making free water directly available for gas/water contact to promote hydrate formation. As shown in Figure 7, this pore filling process occurs at lower water saturation for illite with respect to montmorillonite (Hatch et al., 2012; Sun et al., 2021) because of the strongly bound water in its interlayer spaces; and this could explain the higher induction times in MMT-rich matrix than in ILL at 55% water saturation, the constant induction times in ILL from 55% water saturation and the shorter induction times obtained at higher water saturations in MMT-rich matrix.

These observations are also corroborated by pressure variation (Table 4) at the onset of hydrate formation from one clay to another with the increase in water saturation. The pressure required for hydrate formation in ILL at 55% S_w ranges from 4.81 to 4.98 MPa (Experiments 6_1 to 6_3) while it is in the range of 5.67–6.22 MPa (Experiments 11_1 and 11_2) in the MMT-rich matrix. These higher formation pressures in the MMT-rich matrix are not

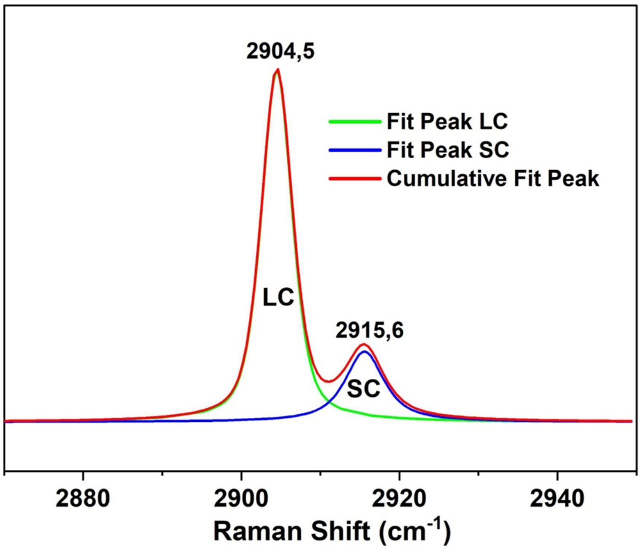

Figure 8. Typical Raman spectra of methane hydrate from 2,860 to 2,950 cm^{-1} showing the signatures of CH_4 trapped in LC (2,904) and small cages (2,915 cm^{-1}) and their deconvolution thanks to the Gauss-Lorentz (Voight) function of the Labspec 5 software.

Table 5

Relative Cage Occupancies, Absolute Cage Occupancies, Hydration Numbers and Gas Storage Capacities Determined for Each Matrix

	Matrix	θ_{LC}/θ_{SC}	θ_{LC} (%)	θ_{SC} (%)	N	GSC or EF (m^3)
	Bulk hydrate	1.10 ± 0.04	97.1 ± 0.3	88.5 ± 3.2	6.06 ± 0.04	163.9 ± 1.0
Sand	Sand	1.14 ± 0.06	97.4 ± 0.3	85.2 ± 4.0	6.09 ± 0.05	162.9 ± 1.4
ILL/Sand	20% Clay	1.23 ± 0,07	97.4 ± 0.3	79.8 ± 4.3	6.17 ± 0.06	159.9 ± 1.5
	40% Clay	1.24 ± 0,08	97.8 ± 0.3	78.6 ± 4.9	6.18 ± 0.07	159.6 ± 1.6
	60% Clay	1.29 ± 0,07	97.8 ± 0.2	76.4 ± 4.7	6.22 ± 0.06	158.7 ± 1.5
MMT/Sand	10% Clay	1.14 ± 0.04	97.8 ± 0.3	85.2 ± 3.4	6.09 ± 0.03	162.9 ± 1.0
	60% Clay	1.18 ± 0.04	97.6 ± 0.1	81.5 ± 2.6	6.13 ± 0.03	160.8 ± 0.9
MMT/ILL	10% MMT/90% ILL	1.26 ± 0.05	97.7 ± 0.2	77.9 ± 3.7	6.19 ± 0.05	159.4 ± 1.2
	30% MMT/70% ILL	1.22 ± 0.05	97.7 ± 0.2	80.1 ± 3.5	6.16 ± 0. 05	160.3 ± 1.1
	53% MMT/47% ILL	1.19 ± 0.06	97.6 ± 0.3	81.7 ± 3.9	6.13 ± 0.05	160.8 ± 1.4

only due to capillarity in small pores but also to the low activity of strongly bound-water as mentioned in previous studies (Clennell et al., 1999; Sun et al., 2021). It is therefore logical that higher pressure levels for hydrate formation onset in MMT matrix at $S_w \leq 55\%$ lead to longer induction times. Similarly, the hydrate formation pressure in the MMT-rich matrix decreases when increasing water saturation from 35% to 100%, resulting in the decrease in induction time. These results are in perfect agreement with the studies of Uchida et al. (2004) and Yakushev (2019), who show that the inhibiting thermodynamic effect (i.e., higher pressure or lower temperature required for hydrate formation) of bentonite clay, associated with the low activity of the strongly adsorbed water and capillarity, vanishes when water saturation reaches 90%. It is important to point out that the MMT used in the present study underwent chemical treatment leading to the leaching of some of the interlayer cations, and its clay fraction is not exclusively composed of smectite (Table 1). This results in a decrease in the swelling capacity compared to an untreated montmorillonite for which the specific surface area is greater and can reach up to 800 m^2/g (Newman, 1983). Thus, we can reasonably speculate that the difference found in the induction time between the two clay used here, and also as a function of water saturation, would have been much more significant.

Previous studies carried out in pure sand did not highlight a clear relationship between induction time and initial water saturation (Benmesbah et al., 2020). Interestingly, induction times from 55% to 82% and at 100% water saturation in ILL and MMT-rich matrix, respectively, are in the same range or lower than the times obtained in pure sand at 55% water saturation. This is related to the fact that the sandy matrix is directly under a pore filling regime at this level of water saturation. However, the induction time for the MMT-rich matrix at $S_w \leq 55\%$ (Figure 6) is 2.5 higher than for pure sand (Figures 5 and 6). These different kinetic behaviors of hydrate formation in sand and clay (in the present study) at different water saturations are clearly linked to the enhanced water/sediment interactions in clays (especially water adsorption on clay particle surfaces and strong binding between water and interlayer cations).

From the results of this set of experiments, we chose a S_w of 75% as an optimum value to synthesize hydrates in different MMT/ILL mixtures (Table 4, Figure 6). Unexpectedly, the values are higher than those obtained in the MMT-rich matrix at 75% S_w. On the other hand, it is worth highlighting that hydrate formation is delayed when the montmorillonite proportion in the matrix is increased from 30% MMT (26.7% smectite) to 53% MMT (44.9% smectite), with the average induction time increasing from 89 to 130.6 min and the average pressure at the hydrate formation onset increasing from 5.71 to 6.83 MPa.

3.3. Effect of Clay on Hydrate Cage Occupancy and Storage Capacity

From the large number of micro-Raman analyses performed, the processing of spectral signatures of CH_4 hydrates (Figure 8) allowed us to describe the variation of the relative cage occupancy, the absolute occupancies of both large and SC, and thus to infer the GSC as a function of the mineralogy of the matrix (Table 5, Figure 9). Since hydrates were formed by pore filling in sand and as veins/lenses in clay-rich matrices (Figure 4),

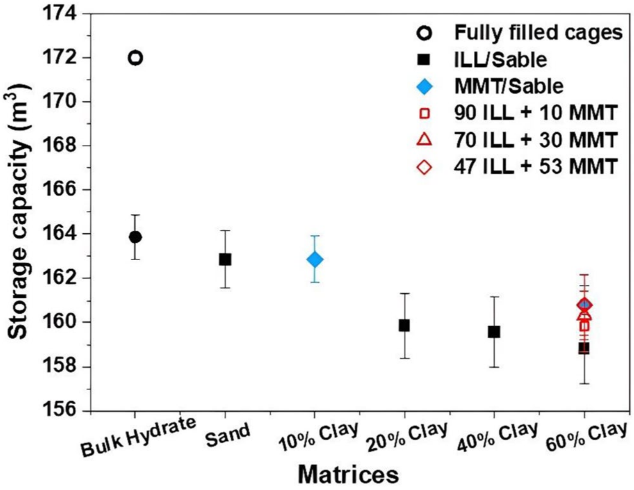

Figure 9. Gas storage capacity of hydrate as a function of matrix mineralogy.

measurements were carried out on sand + hydrate powders and from vein sampling for hydrate-bearing sandy matrix and hydrate-bearing clayey matrices, respectively.

The average relative occupancy obtained for bulk hydrates in this study is 1.10 ± 0.04, which corresponds to an absolute occupancy of 97.1% ± 0.3% of large cages and 88.5% ± 3.2% of SC. These values are in good agreement with those obtained for bulk methane hydrate (θ_{LC}/θ_{SC} ranging from 1.05 to 1.12) in previous studies (Qin & Kuhs, 2013; Sum et al., 1997).

Table 5 shows that the large cages are almost fully occupied with $\theta_{LC} \sim 98\%$ regardless of the mineralogy of the matrix used. However, the SC are partially filled with occupancy fractions decreasing (e.g., increase in the relative cage occupancy) with increasing clay content especially for the ILL/sand mixture. The absolute occupancy of the SC of the hydrate formed in sand ($\theta_{SC} = 85.2\% \pm 4.0\%$) is relatively close to that of the bulk hydrate, while the average value is 76.4% ± 4.7% for the hydrate formed in the ILL/sand matrix (at ~60% clay), for example, a deviation of ~12% (maximum of ~21%) compared to the bulk hydrate. This difference is less significant when the clay used is MMT since small cage occupancy is 85.2% ± 3.4% (similar to sand) and 81.5% ± 2.6% for MMT/sand mixtures with 10% and 60% clay, respectively. Our results indicate that the presence of clay affects the hydrate cage occupancy and it seems to be related to the nature of the clay (Table 5). Conversely (Yeon et al., 2011), found anomalous cage occupancy of natural hydrates disseminated in Na-montmorillonite with θ_{LC}/θ_{SC} up to ~2.40. They show that the mobile interlayer Na^+ cations are inserted into SC during hydrate formation and compete with methane, thereby reducing the absolute occupancy of SC. An analogy might be made with the K^+ ions present in the interlayer space of illite. However, this is unlikely because of the strong interaction between this anhydrous and non-exchangeable cation and the illite sheets that reduce their mobility in the presence of water (which does not enter into the interlayer space) (Dettmann, 1958; Odom & Low, 1978). By increasing the pressure from 3.5 to 15 MPa during bulk methane hydrate formation, Qin and Kuhs found a very slight change in the relative cage occupancy from 1.15 to 1.10, probably related to pressure-dependent change of the relative size of the large and SC (Qin & Kuhs, 2013). Our samples were synthesized under the same temperature and pressure conditions, the only parameter modified during the experiments was the mineralogy of the matrix used. However, a clear explanation cannot be given at this stage on the decrease in absolute occupancy of SC with increasing illite content.

This decrease in the filling rate of SC induces a small decrease in the hydrate storage capacity (Figure 9) ranging from 163.9 ± 1.0 for the bulk hydrate to 158.7 m^3 ± 1.5 in the ILL/sand mixture with 60% clay, that is, a deviation of ~3%. Considering only the minimum and maximum values for bulk hydrate and the hydrate-bearing ILL respectively, a maximum deviation of ~4.5% is reached. From our experiments, the increase in clay content does not significantly affect the GSC of hydrate. However, given the very large volumes of methane stored in hydrate deposits (around 10^{15} m^3), these findings could affect the overall assessment of the amount of methane stored. For comparison, when the cages are completely filled (i.e., $\theta_{LC} = \theta_{LC}$ 100%), the hydrate storage capacity is 172 m^3 and the values that were commonly used in the estimates of methane-in-place volumes in hydrates are 180 (Klauda & Sandler, 2005), 170 (Gornitz & Fung, 1994), or 164 m^3 (K. A. Kvenvolden, 1998). All these values are higher than our values calculated from the micro-Raman spectroscopy analyses.

4. Application to the Black Sea Hydrate Deposits

The Black Sea is the largest isolated sea in the world with an area of 4.23×10^5 km^2. It represents the largest anoxic basin on Earth (Overmann & Manske, 2006), and it is characterized by the occurrence of gas hydrates from the slope sediments to the deep sea (Ker et al., 2019; Klaucke et al., 2006; Popescu et al., 2006; Riboulot et al., 2018). In the Romanian sector of the Black Sea, hydrates are encountered within clay-rich sediments (~60% clays, Table 3) characterized by a relatively diverse mineralogy (illite, smectite, and kaolinite), with depth-variable mineral proportion (Ballas et al., 2018; Ruffine et al., 2021). We performed deep micro-structural characterization of the hydrate-bearing sediments as a function of depth on the collected core GAS-CS05 from the western Black Sea.

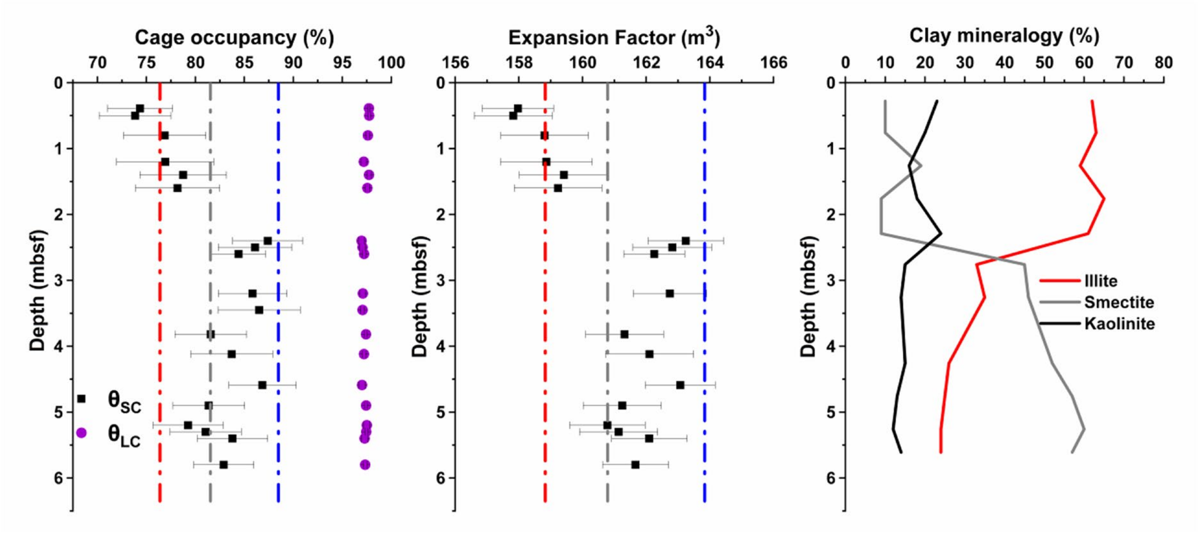

Figure 10. Absolute cage occupancy (left), gas storage capacity (middle), and clay mineralogy (right) of the natural hydrate-bearing sediment samples as a function of depth. The dash dotted lines in the left and middle figures represent the average small cage occupancy and the storage capacity obtained from the synthetic hydrates in the ILL matrix with 77% illite (red), the 53% MMT/47% ILL matrix with ~45% smectite (gray) and the synthetic bulk hydrate (blue).

As for synthetic hydrates, micro-Raman spectroscopy performed on the natural specimens has allowed to obtain the variation of cage occupancy, which in turn enabled to estimate the GSC as summarized in Figure 10. We observed that the large cages are almost fully occupied with θ_{LC} ~98% along the entire length of the core. However, small cage occupancy varies with depth, highlighting two zones (Figure 10a). The first zone is located at less than 2.4 m below sea floor (mbsf) and is characterized by average values of θ_{SC} varying between ~74% and ~78%, which correspond to an average storage capacity between 157.8 and 159.4 m^3. The hydrate samples collected at depth below 2.4 mbsf exhibit more SC occupied by methane. Thus, hydrates have a θ_{SC} ranging between 79.3% and 87.4%, and a resulting storage capacity of around 160.8 and 163.2 m^3, respectively. Interestingly, the horizon located at ~ 2.4 mbsf corresponds to the change in clay mineralogy (Figure 10c), with an illite-rich upper zone (~62% illite) and a lower zone dominated by the presence of smectite (~53%). Our results show a clear link between hydrate cage occupancy and sediment mineralogy: the SC are less occupied in the illite-rich layer compared to the smectite-rich layer. These results are in good agreement with those determined from our investigations from the synthetic cores discussed in the first part of this paper, as shown in Figures 10a and 10b. These figures also present the average values of small cage occupancy and gas storage capacities obtained on the hydrates synthesized in the ILL matrix, the 53% MMT/47% ILL matrix and the bulk synthetic hydrates.

Several estimates of the amount of CH_4 bound as hydrates in the Black Sea (Klauda & Sandler, 2003; Merey & Sinayuc, 2016; Vasilev & Dimitrov, 2003) have been made in the last two decades using different storage capacities. Using an EF of 180 m^3, Klauda and Sandler calculated an amount of methane bound in Black Sea hydrates of 85×10^{13} m^3 (Klauda & Sandler, 2003). A total volume of 71.8×10^{12} m^3 was estimated by Merey and Sinayuc using an EF value of 165.6 m^3 (Merey & Sinayuc, 2016). The difference between these two estimates is mainly related to the methods used to derive hydrate saturation in sediments. However, the Black Sea sediments consist on average of ~60% clay, with illite being the dominant clay mineral (>51%) (Ballas et al., 2018; Huvaj & Huff, 2016; Ruffine et al., 2021; Stoffers & Müller, 1972). Applying to their estimates the average storage capacity of the hydrate in the illite-rich layer (158.7 m^3), determined from our analysis, the total volume estimated is ~11.8% (i.e., 10^{14}) and ~4.6% (i.e., 3.4×10^{12} m^3) less than from those determined by Klauda and Sandler, and Merey and Sinayuc, respectively.

More recently, it has been shown for the Romanian sector of the Black Sea, that salinization triggered the destabilization of shallow gas hydrates, releasing methane that contributes to the current bubble emissions widely observed at the slope area (Riboulot et al., 2018). The authors estimated that, at the scale of the Black Sea, this destabilization could release in the long term up to ~2.1×10^{11} m^3 of CH_4 (EF ~165 m^3) into the water column, with potential impact on marine ecosystems and climate if the gas reaches the atmosphere. We obtained a difference of ∼3.83% (8×10^9 m^3) using a storage capacity of 158.7 m^3. Even if important uncertainties on some parameters inherent to the deposits such as the hydrate saturation in sediments (Vasilev & Dimitrov, 2002) remain to achieve better estimates of methane trapped in hydrate on Earth, it appears from the our study that integrating microscale properties such as cage occupancy and the matrix mineralogy is essential.

5. Conclusions

Experiments of methane hydrate formation were conducted in matrices consisting of mixtures of sand, illite and montmorillonite, with an aim to investigating how matrix mineralogy affects the formation processes. Our results showed that mineralogy significantly affects the formation kinetics and GSC of hydrates. Indeed, clay behaves as a kinetic inhibitor in comparison with sand, as adding only 10% from a sand matrix increases the average induction time by more than 60%. It was also shown that the incipient hydrate formation occurs much faster in illite-rich matrix than in the montmorillonite at low to medium water saturation (35%–55% S_w). This has been attributed to the combined effect of capillarity and the low activity of the strongly bound water in montmorillonite, which significantly reduces the amount of water available for hydrate formation. The effect of water adsorption and capillarity vanished when increasing water saturation in the clayey matrices, leading to a decrease in the induction time at higher water saturations.

Micro-Raman spectroscopy analysis on the synthesized hydrates revealed that increasing the clay content up to ∼60%, in illite in particular, decreases the average small cage occupancy by ∼12% compared to the bulk hydrate. This variation mechanically leads to a decrease in the average GSC that reaches a value of ∼158.7 m^3, lower than those generally used to estimate the amount of hydrate-bound gas. These results on synthetic hydrates were found to be consistent with those obtained from natural hydrate samples collected in the Romanian sector of the Black Sea, and therefore allowed us to revise the estimate of methane trapped in this deposit. Overall, our study shows the importance of considering the effect of the mineralogy of the matrix on hydrate formation kinetics and GSC; key properties to better predict the amount of methane potentially released from hydrate decomposition, either by climate change or anthropogenic operations for natural gas production.

Data Availability Statement

The data of sediments characterization, pressure, and temperature from high pressure experiments for hydrate synthesis, and of hydrate cage occupancy and storage capacity, are available in Mendeley Data (https://data.mendeley.com/, Agnissan, 2023).

Acknowledgments

The authors also acknowledge Phillippe Fernagu, Mickael Rovere, and Nicolas Gayet for their technical support in hydrate sampling prior to micro-Raman spectroscopy and SEM analyses, respectively. All Raman experiments have been performed at the platform SIV at University of Bordeaux, funded by the University of Bordeaux, the FEDER, and the Region "Nouvelle Aquitaine" (AAPPF2022-2021-16611310). David Talaga and Jean-Luc Bruneel are thanked for their technical support during the Raman measurements. The authors also thank the various projects and programmes for their financial support (H2020-DOORS/Project 101000518, the project NANOCLAY co-funded by Region "Nouvelle Aquitaine," the Doctoral Fellowship program of the Scientific Direction of Ifremer and the ANR project HYDRACLAY ANR-22-CE29-0025-01 and BLAME ANR-18-CE01-0007, funded by the French National Research Agency). We also acknowledge Alison Chalm for proofreading the article.

References

Agnissan, C. (2023). Influence of clay-rich sediments on methane hydrate formation: Impacts on kinetic behaviour and gas storage capacity - Database. Mendeley Data, V1. https://doi.org/10.17632/m4v5hrnv2z.1

Babu, P., Yee, D., Linga, P., Palmer, A., Khoo, B. C., Tan, T. S., & Rangsunvigit, P. (2013). Morphology of methane hydrate formation in porous media. *Energy & Fuels*, *27*(6), 3364–3372. https://doi.org/10.1021/ef4004818

Bagherzadeh, S. A., Moudrakovski, I. L., Ripmeester, J. A., & Englezos, P. (2011). Magnetic resonance imaging of gas hydrate formation in a bed of silica sand particles. *Energy & Fuels*, *25*(7), 3083–3092. https://doi.org/10.1021/ef200399a

Ballas, G., Garziglia, S., Sultan, N., Pelleter, E., Toucanne, S., Marsset, T., et al. (2018). Influence of early diagenesis on geotechnical properties of clay sediments (Romania, Black Sea). *Engineering Geology*, *240*, 175–188. https://doi.org/10.1016/j.enggeo.2018.04.019

Benmesbah, F. D., Ruffine, L., Clain, P., Osswald, V., Fandino, O., Fournaison, L., & Delahaye, A. (2020). Methane hydrate formation and dissociation in sand media: Effect of water saturation, gas flowrate and particle size. *Energies*, *13*(19), 5200. https://doi.org/10.3390/en13195200

Boswell, R., & Collett, T. (2011). Current perspectives on gas hydrate resources. *Energy & Environmental Science*, *4*, 1206–1215. https://doi.org/10.1039/c0ee00203h

Boswell, R., Hancock, S., Yamamoto, K., Collett, T., Pratap, M., & Lee, S.-R. (2020). 6 - Natural gas hydrates: Status of potential as an energy resource. In T. M. Letcher (Ed.), *Future energy* (3rd ed., pp. 111–131). Elsevier.

Cases, J. M., Berend, I., Besson, G., Francois, M., Uriot, J. P., Thomas, F., & Poirier, J. E. (1992). Mechanism of adsorption and desorption of water vapor by homoionic montmorillonite. 1. The sodium-exchanged form. *Langmuir*, *8*(11), 2730–2739. https://doi.org/10.1021/la00047a025

Chazallon, B., Rodriguez, C. T., Ruffine, L., Carpentier, Y., Donval, J. P., Ker, S., & Riboulot, V. (2020). Characterizing the variability of natural gas hydrate composition from a selected site of the Western Black Sea, off Romania. *Marine and Petroleum Geology*, *124*, 104785. https://doi.org/10.1016/j.marpetgeo.2020.104785

Chong, Z. R., Yang, M., Khoo, B. C., & Linga, P. (2016). Size effect of porous media on methane hydrate formation and dissociation in an excess gas environment. *Industrial & Engineering Chemistry Research*, *55*(29), 7981–7991. https://doi.org/10.1021/acs.iecr.5b03908

Chuvilin, E., Perlova, E. V., Makhonina, N. A., Yakushev, V. S., & Dubinyak, D. V. (2002). Peculiarities of methane hydrate formation/dissociation P/T conditions in sediments of different composition. In *Proceeding of 4-th international conference on gas hydrates*.

Clennell, M. B., Hovland, M., Booth, J. S., Henry, P., & Winters, W. J. (1999). Formation of natural gas hydrates in marine sediments: 1. Conceptual model of gas hydrate growth conditioned by host sediment properties. *Journal of Geophysical Research*, *104*(B10), 22985–23003. https://doi.org/10.1029/1999JB900175

Dai, S., Santamarina, J. C., Waite, W. F., & Kneafsey, T. J. (2012). Hydrate morphology: Physical properties of sands with patchy hydrate saturation. *Journal of Geophysical Research*, *117*(B11), B11205. https://doi.org/10.1029/2012JB009667

Das, B. M. (2008). *Advanced soil mechanics*. Taylor & Francis.

Davidson, D. W., Desando, M. A., Gough, S. R., Handa, Y. P., Ratcliffe, C. I., Ripmeester, J. A., & Tse, J. S. (1987). Some physical and thermophysical properties of clathrate hydrates. *Journal of Inclusion Phenomena*, *5*(2), 219–223. https://doi.org/10.1007/BF00655652

Davidson, D. W., Handa, Y. P., & Ripmeester, J. A. (1986). Xenon-129 NMR and the thermodynamic parameters of xenon hydrate. *The Journal of Physical Chemistry*, *90*(24), 6549–6552. https://doi.org/10.1021/j100282a026

Desmedt, A., Bedouret, L., Pefoute, E., Pouvreau, M., Say-Liang-Fat, S., & Alvarez, M. (2012). Energy landscape of clathrate hydrates. *The European Physical Journal Special Topics*, *213*(1), 103–127. https://doi.org/10.1140/epjst/e2012-01666-3

Dettmann, M. G. (1958). Water uptake by pure clays and soil crumbs. *Journal of Soil Science*, *9*(2), 306–315. https://doi.org/10.1111/j.1365-2389.1958.tb01922.x

Dickens, G. R., Castillo, M. M., & Walker, J. C. G. (1997). A blast of gas in the latest Paleocene: Simulating first-order effects of massive dissociation of oceanic methane hydrate. *Geology*, *25*(3), 259–262. https://doi.org/10.1130/0091-7613(1997)025<0259:ABOGIT>2.3.CO;2

Fütterer, D. K. (2006). The solid phase of marine sediments. In H. D. Schulz & M. Zabel (Eds.), *Marine geochemistry* (pp. 1–25). Springer Berlin Heidelberg.

Gornitz, V., & Fung, I. (1994). Potential distribution of methane hydrates in the world's oceans. *Global Biogeochemical Cycles*, *8*(3), 335–347. https://doi.org/10.1029/94GB00766

Grim, R. E. (1962). *Applied clay mineralogy*. McGraw-Hill Ed.

Hancock, S., Dallimore, S., Collett, T., Carle, D., Weatherill, B., & Satoh, T. (2005). *Mallik 5L-38 gas hydrate production research well* (p. 585). Bulletin/Geological Survey Canada.

Handa, Y. P., & Stupin, D. Y. (1992). Thermodynamic properties and dissociation characteristics of methane and propane hydrates in 70-.ANG.-radius silica gel pores. *The Journal of Physical Chemistry*, *96*(21), 8599–8603. https://doi.org/10.1021/j100200a071

Hatch, C. D., Wiese, J. S., Crane, C. C., Harris, K. J., Kloss, H. G., & Baltrusaitis, J. (2012). Water adsorption on clay minerals as a function of relative humidity: Application of BET and Freundlich adsorption models. *Langmuir*, *28*(3), 1790–1803. https://doi.org/10.1021/la2042873

Heeschen, K. U., Schicks, J. M., & Oeltzschner, G. (2016). The promoting effect of natural sand on methane hydrate formation: Grain sizes and mineral composition. *Fuel*, *181*, 139–147. https://doi.org/10.1016/j.fuel.2016.04.017

Holland, M., Schultheiss, P., Roberts, J., & Druce, M. (2008). Observed gas hydrate morphologies in marine sediments.

Holtz, R. D., Kovacs, W. D., & Sheahan, T. C. (2011). An introduction to geotechnical engineering (2nd ed.).

Huvaj, Y. N., & Huff, W. (2016). Clay mineralogy and geochemistry of three offshore wells in the southwestern Black Sea, northern Turkey: The effect of burial diagenesis on the conversion of smectite to illite. *Turkish Journal of Earth Sciences*, *25*, 592–610. https://doi.org/10.3906/yer-1601-10

Kennett, J. P., Cannariato, K. G., Hendy, I. L., & Behl, R. J. (2003). Methane hydrates in quaternary climate change: The clathrate gun hypothesis. In *Special publications series, American geophysical union* (Vol. 54). Wiley Online Library.

Ker, S., Thomas, Y., Riboulot, V., Sultan, N., Bernard, C., Scalabrin, C., et al. (2019). Anomalously deep BSR related to a transient state of the gas hydrate system in the western Black Sea. *Geochemistry, Geophysics, Geosystems*, *20*(1), 442–459. https://doi.org/10.1029/2018GC007861

Klapproth, A., Techmer, K., Klapp, S., Murshed, M., & Kuhs, W. (2006). Microstructure of gas hydrates in porous media. In *Paper presented at the 11th international conference on the physics and chemistry of ice (PCI-2006)*.

Klaucke, I., Sahling, H., Weinrebe, W., Blinova, V., Bürk, D., Lursmanashvili, N., & Bohrmann, G. (2006). Acoustic investigation of cold seeps offshore Georgia, eastern Black Sea. *Marine Geology*, *231*(1), 51–67. https://doi.org/10.1016/j.margeo.2006.05.011

Klauda, J. B., & Sandler, S. (2005). Global distribution of methane hydrate in ocean sediment. *Energy & Fuels*, *19*(2), 459–470. https://doi.org/10.1021/ef049798o

Klauda, J. B., & Sandler, S. I. (2003). Predictions of gas hydrate phase equilibria and amounts in natural sediment porous media. *Marine and Petroleum Geology*, *20*(5), 459–470. https://doi.org/10.1016/s0264-8172(03)00064-3

Koh, C. A., Sum, A. K., & Sloan, E. D. (2012). State of the art: Natural gas hydrates as a natural resource. *Journal of Natural Gas Science and Engineering*, *8*, 132–138. https://doi.org/10.1016/j.jngse.2012.01.005

Kumar, A., Sakpal, T., Roy, S., & Kumar, R. (2015). Methane hydrate formation in a test sediment of sand and clay at various level of water saturation. *Canadian Journal of Chemistry*, *93*, 1–8. https://doi.org/10.1139/cjc-2014-0537

Kumari, N., & Mohan, C. (2021). Basics of clay minerals and their characteristic properties. In N. Gustavo Morari Do (Ed.), *Clay and clay minerals*. IntechOpen.

Kvenvolden, K. A. (1998). A primer on the geological occurrence of gas hydrate. *Geological Society, London, Special Publications*, *137*(1), 9–30. https://doi.org/10.1144/GSL.SP.1998.137.01.02

Lee, J. Y., Santamarina, J. C., & Ruppel, C. (2008). Mechanical and electromagnetic properties of northern Gulf of Mexico sediments with and without THF hydrates. *Marine and Petroleum Geology*, *25*(9), 884–895. https://doi.org/10.1016/j.marpetgeo.2008.01.019

Lei, L., & Santamarina, J. (2018). Laboratory strategies for hydrate formation in fine-grained sediments. *Journal of Geophysical Research: Solid Earth*, *123*(4), 2583–2596. https://doi.org/10.1002/2017jb014624

Levin, L. A. (2005). Ecology of cold seep sediments: Interactions of fauna with flow, chemistry and microbes. *Oceanography and Marine Biology*, *43*, 11–56.

Linga, P., Haligva, C., Nam, S., Ripmeester, J., & Englezos, P. (2009). Gas hydrate formation in a variable volume bed of silica sand particles. *Energy & Fuels*, *23*(11), 5496–5507. https://doi.org/10.1021/ef900542m

Linga, P., Kumar, R., & Englezos, P. (2007). The clathrate hydrate process for post and pre-combustion capture of carbon dioxide. *Journal of Hazardous Materials*, *149*(3), 625–629. https://doi.org/10.1016/j.jhazmat.2007.06.086

Liu, C., Lu, H., Ye, Y., Ripmeester, J. A., & Zhang, X. (2008). Raman spectroscopic observations on the structural characteristics and dissociation behavior of methane hydrate synthesized in silica sands with various sizes. *Energy & Fuels*, *22*(6), 3986–3988. https://doi.org/10.1021/ef800440s

Loh, M., Falser, S., Babu, P., Linga, P., Palmer, A., & Tan, T.-S. (2012). Dissociation of fresh- and seawater hydrates along the phase boundaries between 2.3 and 17 MPa. *Energy & Fuels*, *26*(10), 6240–6246. https://doi.org/10.1021/ef3008954

MacDonald, I. R., Sager, W. W., & Peccini, M. B. (2003). Gas hydrate and chemosynthetic biota in mounded bathymetry at mid-slope hydrocarbon seeps: Northern Gulf of Mexico. *Marine Geology*, *198*(1), 133–158. https://doi.org/10.1016/s0025-3227(03)00098-7

Malagar, B. R. C., Lijith, K. P., & Singh, D. N. (2019). Formation & dissociation of methane gas hydrates in sediments: A critical review. *Journal of Natural Gas Science and Engineering*, *65*, 168–184. https://doi.org/10.1016/j.jngse.2019.03.005

Martin, R. T. (1960). Adsorbed water on clay: A review. *Clays and Clay Minerals*, *9*(1), 28–70. https://doi.org/10.1346/CCMN.1960.0090104

Mekala, P., Babu, P., Sangwai, J. S., & Linga, P. (2014). Formation and dissociation kinetics of methane hydrates in seawater and silica sand. *Energy & Fuels*, *28*(4), 2708–2716. https://doi.org/10.1021/ef402445k

Merey, Ş., & Sinayuc, C. (2016). Investigation of gas hydrate potential of the Black Sea and modelling of gas production from a hypothetical Class 1 methane hydrate reservoir in the Black Sea conditions. *Journal of Natural Gas Science and Engineering*, *29*, 66–79. https://doi.org/10.1016/j.jngse.2015.12.048

Milkov, A. (2004). Global estimates of hydrate-bound gas in marine sediments: How much is really out there? *Earth-Science Reviews*, *66*(3–4), 183–197. https://doi.org/10.1016/j.earscirev.2003.11.002

Nakayama, T., Tomura, S., Ozaki, M., Ohmura, R., & Mori, Y. H. (2010). Engineering investigation of hydrogen storage in the form of clathrate hydrates: Conceptual design of hydrate production plants. *Energy & Fuels*, *24*(4), 2576–2588. https://doi.org/10.1021/ef100039a

Newman, A. C. D. (1983). The specific surface of soils determined by water sorption. *European Journal of Soil Science*, *34*(1), 23–32. https://doi.org/10.1111/j.1365-2389.1983.tb00809.x

Odom, J. W., & Low, P. F. (1978). Relation between swelling, surface area and b dimension of Na-montmorillonites. *Clays and Clay Minerals*, *26*(5), 345–351. https://doi.org/10.1346/CCMN.1978.0260505

Østergaard, K. K., Anderson, R., Llamedo, M., & Tohidi, B. (2002). Hydrate phase equilibria in porous media: Effect of pore size and salinity. *Terra Nova*, *14*(5), 307–312. https://doi.org/10.1046/j.1365-3121.2002.00433.x

Overmann, J., & Manske, A. K. (2006). Anoxygenic phototrophic bacteria in the black sea chemocline. In *Paper presented at the past and present water column anoxia*.

Park, J., & Santamarina, J. (2017). Revised soil classification system for coarse-fine mixtures. *Journal of Geotechnical and Geoenvironmental Engineering*, *143*(8), 04017039. https://doi.org/10.1061/(asce)gt.1943-5606.0001705

Popescu, I., De Batist, M., Lericolais, G., Nouzé, H., Poort, J., Panin, N., et al. (2006). Multiple bottom-simulating reflections in the Black Sea: Potential proxies of past climate conditions. *Marine Geology*, *227*(3), 163–176. https://doi.org/10.1016/j.margeo.2005.12.006

Qin, J., & Kuhs, W. F. (2013). Quantitative analysis of gas hydrates using Raman spectroscopy. *AIChE Journal*, *59*(6), 2155–2167. https://doi.org/10.1002/aic.13994

Riboulot, V., Ker, S., Sultan, N., Thomas, Y., Marsset, B., Scalabrin, C., et al. (2018). Freshwater lake to salt-water sea causing widespread hydrate dissociation in the Black Sea. *Nature Communications*, *9*(1), 117. https://doi.org/10.1038/s41467-017-02271-z

Ruffine, L. (2015). Exploring methane-hydrate formation and dissociation in geologic materials through laboratory experiments: Kinetic behavior and morphology. *Fuel*, *141*, 173–184. https://doi.org/10.1016/j.fuel.2014.10.041

Ruffine, L., Broseta, D., & Desmedt, A. (2018). *Gas hydrates 2: Geoscience issues and potential industrial applications*. Wiley.

Ruffine, L., Deusner, C., Haeckel, M., Kossel, E., Toucanne, S., Chéron, S., et al. (2021). Effects of postglacial seawater intrusion on sediment geochemical characteristics in the Romanian sector of the Black Sea. *Marine and Petroleum Geology*, *123*, 104746. https://doi.org/10.1016/j.marpetgeo.2020.104746

Ruppel, C. D., & Kessler, J. D. (2017). The interaction of climate change and methane hydrates. *Reviews of Geophysics*, *55*(1), 126–168. https://doi.org/10.1002/2016RG000534

Santamarina, J. C., Klein, A., & Fam, M. A. (2001). Soils and waves: Particulate materials behavior, characterization and process monitoring. *Journal of Soils and Sediments*, *1*(2), 130. https://doi.org/10.1007/bf02987719

Schuttlefield, J. D., Cox, D., & Grassian, V. H. (2007). An investigation of water uptake on clays minerals using ATR-FTIR spectroscopy coupled with quartz crystal microbalance measurements. *Journal of Geophysical Research*, *112*(D21), D21303. https://doi.org/10.1029/2007JD008973

Seol, J., Lee, J.-W., Kim, D.-Y., Takeya, S., Ripmeester, J. A., & Lee, H. (2010). Molecular cage occupancy of clathrate hydrates at infinite dilution: Experimental determination and thermodynamic significance. *The Journal of Physical Chemistry B*, *114*(2), 804–808. https://doi.org/10.1021/jp909982n

Seol, J., Shin, W., Koh, D.-Y., Kang, H., Sung, B., & Lee, H. (2012). Spectroscopic observation of Na cations entrapped in small cages of sII propane hydrate. *Journal of Physical Chemistry C*, *116*(1), 1439–1444. https://doi.org/10.1021/jp207450e

Shmulovich, K., Yardley, B., & Gonchar, G. (1994). *Fluids in the crust: Equilibrium and transport properties*. Springer Science & Business Media.

Sloan, E. D., Jr., & Koh, C. A. (2007). *Clathrate hydrates of natural gases*. CRC Press.

Stoffers, P., & Müller, p. (1972). Clay mineralogy of black sea sediments. *Sedimentology*, *18*(1–2), 113–121. https://doi.org/10.1111/j.1365-3091.1972.tb00006.x

Sultan, N., Cochonat, P., Foucher, J. P., & Mienert, J. (2004). Effect of gas hydrates melting on seafloor slope instability. *Marine Geology*, *213*(1), 379–401. https://doi.org/10.1016/j.margeo.2004.10.015

Sum, A. K., Burruss, R. C., & Sloan, E. D. (1997). Measurement of clathrate hydrates via Raman spectroscopy. *The Journal of Physical Chemistry B*, *101*(38), 7371–7377. https://doi.org/10.1021/jp970768e

Sun, Y., Jiang, S., Li, S., Wang, X., & Peng, S. (2021). Hydrate formation from clay bound water for CO_2 storage. *Chemical Engineering Journal*, *406*, 126872. https://doi.org/10.1016/j.cej.2020.126872

Terzariol, M., Park, J., Castro, G. M., & Santamarina, J. C. (2020). Methane hydrate-bearing sediments: Pore habit and implications. *Marine and Petroleum Geology*, *116*, 104302. https://doi.org/10.1016/j.marpetgeo.2020.104302

Terzariol, M., Sultan, N., Apprioual, R., & Garziglia, S. (2021). Pore habit of gas in gassy sediments. *Journal of Geophysical Research: Solid Earth*, *126*(5), e2020JB021511. https://doi.org/10.1029/2020jb021511

Trofimuk, A., Cherskiy, N. V., & Tsarev, V. P. (1975). The biogenic methane resources in the oceans. *Doklady Akademii Nauk SSSR*, *225*.

Tulk, C. A., Ripmeester, J. A., & Klug, D. D. (2006). The application of Raman spectroscopy to the study of gas hydrates. *Annals of the New York Academy of Sciences*, *912*(1), 859–872. https://doi.org/10.1111/j.1749-6632.2000.tb06840.x

Uchida, T., Ebinuma, T., Takeya, S., Nagao, J., & Narita, H. (2002). Effects of pore sizes on dissociation temperatures and pressures of methane, carbon dioxide, and propane hydrates in porous media. *The Journal of Physical Chemistry B*, *106*(4), 820–826. https://doi.org/10.1021/jp012823w

Uchida, T., Takeya, S., Chuvilin, E. M., Ohmura, R., Nagao, J., Yakushev, V. S., et al. (2004). Decomposition of methane hydrates in sand, sandstone, clays, and glass beads. *Journal of Geophysical Research*, *109*(B5), B05206. https://doi.org/10.1029/2003JB002771

Vasilev, A., & Dimitrov, L. (2002). Spatial and quantitative evaluation of the Black Sea gas hydrates. *Geologiya i Geofizika*, *43*, 672–684.

Vasilev, A., & Dimitrov, L. (2003). Model evaluation of the Black Sea gas hydrates. *Comptes Rendus de l'Academie Bulgare des Sciences*, *56*, 15.

Vavra, C. L., Kaldi, J., & Sneider, R. M. (1992). Geological applications of capillary pressure: A review. *AAPG Bulletin*, *76*, 840–850.

Waals, J. H. V. D., & Platteeuw, J. C. (1958). Clathrate solutions. In I. Prigogine (Ed.), *Advances in chemical physics* (pp. 1–57).

Wallmann, K., Piñero, E., Burwicz, E., Haeckel, M., Hensen, C., Dale, A., & Ruepke, L. (2012). The global inventory of methane hydrate in marine sediments: A theoretical approach. *Energies*, *5*(7), 2449–2498. https://doi.org/10.3390/en5072449

Wang, H., Qian, H., Gao, Y., & Li, Y. (2020). Classification and physical characteristics of bound water in loess and its main clay minerals. *Engineering Geology*, *265*, 105394. https://doi.org/10.1016/j.enggeo.2019.105394

Wang, S., Yang, M., Liu, W., Zhao, J., & Song, Y. (2016). Investigation on the induction time of methane hydrate formation in porous media under quiescent conditions. *Journal of Petroleum Science and Engineering*, *145*, 565–572. https://doi.org/10.1016/j.petrol.2016.06.003

Weil, R., & Brady, N. (2017). The nature and properties of soils (15th ed.).

Xu, W., & Ruppel, C. (1999). Predicting the occurrence, distribution, and evolution of methane gas hydrate in porous marine sediments. *Journal of Geophysical Research*, *104*(B3), 5081–5095. https://doi.org/10.1029/1998JB900092

Yakushev, V. S. (2019). Experimental modeling of methane hydrate formation and decomposition in wet heavy clays in arctic regions. *Geosciences*, *9*(1), 13. https://doi.org/10.3390/geosciences9010013

Yamamoto, K., Wang, X. X., Tamaki, M., & Suzuki, K. (2019). The second offshore production of methane hydrate in the Nankai Trough and gas production behavior from a heterogeneous methane hydrate reservoir. *RSC Advances*, *9*(45), 25987–26013. https://doi.org/10.1039/C9RA00755E

Yeon, S.-H., Seol, J., Koh, D.-Y., Seo, Y.-J., Park, K.-P., Huh, D.-G., et al. (2011). Abnormal methane occupancy of natural gas hydrates in deep sea floor sediments. *Energy & Environmental Science*, *4*(2), 421–424. https://doi.org/10.1039/C0EE00355G

You, K., Flemings, P. B., Malinverno, A., Collett, T. S., & Darnell, K. (2019). Mechanisms of methane hydrate formation in geological systems. *Reviews of Geophysics*, *57*(4), 1146–1196. https://doi.org/10.1029/2018RG000638

Zeng, H., Zhang, Y., Zhang, L., Chen, Z., & Li, X. (2022). Effects of the NaCl concentration and montmorillonite content on formation kinetics of methane hydrate. *Journal of Marine Science and Engineering*, *10*(4), 548. https://doi.org/10.3390/jmse10040548

Zhang, L., Xu, S., Li, X., Zhang, Y., Yang, R., Ouyang, Q., & Ren, S. (2017). Reaction kinetic characteristics and model of methane hydrate formation in porous media. *Energy & Fuels*, *31*(8), 8548–8559. https://doi.org/10.1021/acs.energyfuels.7b00958